Comparative Analysis of Advanced Machine Learning Methods for Heat Transfer and Thermal Efficiency in a Non-Newtonian Nanofluid with Joule Heating and Lorentz Forces: Dual Solutions and Stability Analysis

Suad Alrebdi[1], Umair Khan[2,3,*], Rania Saadeh[4] and Aurang Zaib[5]

[1] Department of Entrepreneurship, Entrepreneurship Institute, King Saud University, Riyadh, Saudi Arabia

[2] Department of Mathematics Saveetha School of Engineering, Saveetha Institute of Medical and Technical Sciences, Saveetha University, Chennai, India

[3] Department of Mathematics, Faculty of Science, Sakarya University, Serdivan/Sakarya, Turkey

[4] Department of Applied Science, Ajloun College, Al-Balqa Applied University, Ajloun, Jordan

[5] Department of Mathematics, University of Karachi, Karachi, Pakistan

INFORMATION

Keywords:
Advanced machine learning
convective boundary condition
second-grade fluid
Joule heating
unsteady flow

DOI: 10.23967/j.rimni.2026.10.75620

SCIPEDIA Revista Internacional de Métodos Numéricos para Cálculo y Diseño en Ingeniería

Revista Internacional Métodos numéricos para cálculo y diseño en ingeniería RIMNI

In cooperation with CIMNE

Comparative Analysis of Advanced Machine Learning Methods for Heat Transfer and Thermal Efficiency in a Non-Newtonian Nanofluid with Joule Heating and Lorentz Forces: Dual Solutions and Stability Analysis

Suad Alrebdi[1], Umair Khan[2,3,*], Rania Saadeh[4] and Aurang Zaib[5]

[1]Department of Entrepreneurship, Entrepreneurship Institute, King Saud University, Riyadh, Saudi Arabia

[2]Department of Mathematics Saveetha School of Engineering, Saveetha Institute of Medical and Technical Sciences, Saveetha University, Chennai, India

[3]Department of Mathematics, Faculty of Science, Sakarya University, Serdivan/Sakarya, Turkey

[4]Department of Applied Science, Ajloun College, Al-Balqa Applied University, Ajloun, Jordan

[5]Department of Mathematics, University of Karachi, Karachi, Pakistan

ABSTRACT

This research explores the unsteady stagnation point flow of modified second-grade fluid by incorporating magnetized cobalt ferrite ($CoFe_2O_4$) nanoparticles across a heated movable plate. In addition, the radiation and Joule heating are also provoked. Since the cobalt ferrite particles are very important in biosensing, drug delivery, magnetic purification/separation, etc. The leading equations are changed into ordinary differential equations by employing similarity factors and then utilizing the bvp4c solver to obtain dual numerical solutions. Stability analysis confirms that the upper branch solution is stable and physically reliable. In addition, this research is further analyzed through advanced machine learning by employing artificial neural networks in conjunction with Levenberg-Marquardt. Moreover, this research deals with an important query by computing the problem through Gaussian Process Regression (GPR). The substantial outcomes indicate the velocity increases while the temperature declines due to the viscosity factor for the upper solution. In parallel, the machine learning outcomes show that the GPR gets an excellent R^2 of 1 and, for the Nusselt number prediction, delivers a predictive error within the same order of magnitude as the ANN-LM benchmark. This confirms GPR as a high-fidelity tool capable of achieving near-perfect accuracy, making it a powerful choice where both precision and predictive confidence are essential.

OPEN ACCESS

Received: 05/11/2025

Accepted: 04/01/2026

Published: 20/03/2026

DOI
10.23967/j.rimni.2026.10.75620

Keywords:
Advanced machine learning
convective boundary condition
second-grade fluid
Joule heating
unsteady flow

1 Introduction

The exploration of the boundary-layer flow of non-Newtonian fluids has attracted a lot of interest from scientists and researchers because these fluids are frequently utilized in industries. Some recognized examples are blood, polymer solutions, polymer melts, and paints. Generally, determining

*Correspondence: Umair Khan (umairkhan@sakarya.edu.tr).

the properties of all the non-Newtonian fluids using a single constitutive equation is quite difficult. Plenty of studies have been made on the second-grade liquid according to Rivlin and Erickson [1]. The fluid model discovers the penalty of the convectional stress. Vajravelu and Rollins [2] examined the flow trend of the second-grade liquid subject to a stretchable surface with Lorentz force. Their results suggested that the second-grade liquid could be exploited in metallurgy and polymer technologies. Throughout metallurgical procedures, enormous, unending filaments or strips to simulate extensive sheets must be cooled in a sluggish liquid. Vajravelu and Roper [3] scrutinized the flow of second-grade liquid across a stretchable sheet and obtained the unique solution by involving an extra boundary situation. The slip constraint impact on the flow of second-grade liquid via a solid wall was examined by Labropulu and Li [4]. Khan and Rahman [5] analyzed the trend of a special second-grade liquid induced by an asymmetrical isothermal stretched sheet. Ramzan et al. [6] discussed the buoyancy impact on the radiative flow of a second-grade liquid via a stretchable exponential plate. Labropulu and Li [7] examined the time-dependent stagnation point flow of second-grade liquid and heat transfer across a boundless plate. Their results revealed that the velocity turns down due to the Weissenberg number near the wall. Saif et al. [8] scrutinized the stagnation point flow of second-grade nanofluid across an asymmetrical stretched surface. Their results revealed that the concentration and temperature strengthened due to the thermophoresis effect. Awan et al. [9] inspected the effect of a magnetic field on the unsteady flow of second-grade liquid towards an oblique stagnation point through an oscillatory stretchable sheet. They found that the friction factor increases due to the magnetic number and decline due to the Weissenberg number. Salahuddin et al. [10] studied the irregular viscosity effect on the squeezing flow of a second-grade nanoliquid bounded via an unbounded channel with heat generation. Their outcomes revealed that the velocity increases due to the squeezing factor and reduces due to the fluid factor. Khashi'ie et al. [11] explored the significance of the second-grade liquid through water-based nanoliquid past a movable Riga plate. A unique solution is obtained for stretching and static cases, while multiple solutions are observed for certain values of suction. The magnetic impact of the flow of second-grade liquid across a stretching curved surface was inspected by Hosseinzadeh et al. [12]. It is seen that the skin friction uplifts due to the second-grade factor.

The convectional liquids of heat transport, like water, oil, and ethylene glycol, have reasonably poor thermal efficiency, contrary to the bulk of firm materials. Generally, these liquids are deployed as a heat provider in the heat transport apparatus. Heat transport is implemented via a heat exchanger in the solo phase, as well as multiphase flow applications, which correspond to an important industrial procedure. To advance the efficiency of thermal resistivity is one of the several attempts performed in recent times to improve the phenomenon of heat transport. Choi and Eastman [13] took the preliminary research on the study of nanoliquids and their capability to scatter nano-scale particles in conventional liquids. Mahdy [14] inspected the unsteady flow of nanofluid across a stretchable sheet with thermal conductivity and dynamic viscosity. It is concluded that the fluid temperature increases while the velocity shrinks in the presence of nanofluid. Sheikholeslami et al. [15] explored the magnetic effect on the free convective flow of nanoliquid with radiation effects. Soid et al. [16] scrutinized the two-dimensional time-dependent flow of nanoliquid across a needle, and dual outcomes were presented. Kamal et al. [17] explored the significance of nanoliquid alongside a moving sheet with a chemical reaction. The impact of radiation on the free convective flow of water-based single-walled carbon nanotubes in a porous medium with a magnetic field was explored by Al-Kouz et al. [18]. Their results predicted that the Nusselt number demonstrates a diminishing trend due to the magnetic number and growing behavior due to nanoparticle volume fraction. Khan et al. [19] inspected the 2D flow and heat transport by engaging a nanoliquid across a porous surface saturated in a porous

medium. Khan et al. [20] analyzed the mixed convective flow of micropolar hybrid nanofluids past a vertical permeable stretching sheet with melting heat transfer and thermal radiation effects. Their computational results suggested that the temperature profile and heat transfer rate increase with higher values of the thermal radiation parameter. Yu et al. [21] investigated the 3D flow of nanoliquid from a flat sheet in a porous medium with a modified slip effect. Their results revealed that the velocity improves notably in the first and second solutions due to the porous parameter. Elattar et al. [22] explored the impact of entropy generation via the cross-radiative flow of nanofluid subject to a movable surface with a heat sink/source. Their outcome discovered that the heat transport shrinks and enhances owing to the heat sink and heat source, respectively. Recently, Dawod et al. [23] analyzed the three-dimensional time-dependent flow of nanoliquid across a plane flat sheet with the trend of the bioconvection flow. Their findings demonstrated that the velocity exhibits a growing behavior in the condition of the nodal tip in both directions.

The problems containing the flow and heat transport induced by convective boundary constraints are employed in distinct engineering fields like substance processing, discovery of geothermal energy, cooling of industrial equipment, etc. The Buongiorno model of nanofluid on a stretchable surface with convective boundary constraint was explored by Makinde and Aziz [24]. Their results revealed that the fluid temperature increases in the presence of the Biot number. Alsaedi et al. [25] examined the impact of convective boundary constraint on the nanofluid flow towards a stagnation point across a porous stretched sheet with heat absorption/generation. They observed that the temperature increases due to the Biot number. Ibrahim [26] inspected the convective boundary constraint on the magneto flow of Maxwell liquid by considering nanofluid past a flexible sheet with an induced magnetic field. The influence of substance reaction on the MHD flow of Powell-Eyring nanofluid induced by a Riga plate with radiation and convective boundary condition was explored by Rasool and Zhang [27]. Their outcomes revealed that the magnetic number plays a considerable role in the profile of fluid flow in the presence of the Riga plate. Baitharu et al. [28] scrutinized the thermal slip effect on the free convective flow of polar fluid over an elevated concentric cylinder with convective boundary conditions. It is observed that the thermal slip effect negatively influences the uniqueness of polar fluid. Rashad et al. [29] discussed the 2D magneto flow of hybrid Williamson nanofluids past a curved surface with convective boundary constraint. They monitored the skin friction uplifts due to radiation and the Biot number. Recently, Ahmed et al. [30] studied the bioconvection flow towards a stagnation point past a stretching sheet with nanofluid, convective boundary constraint, and heat sink/source. Their results indicated that the temperature improves in the presence of the Biot number and the heat source.

Heat transport is identified as an exchange of heat within physical systems that have distinct temperatures. This can be produced through conduction, radiation, or convection. However, amongst them, radiation is a much better route for heat transport. Thermal radiation is important when it comes to heat transport and fluid dynamics studies. The word thermal radiation occurs only in the scenario of thermal energy by means of a large velocity gradient. The flow and mechanisms of heat transfer with thermal radiation play a significant role in technology such as gas turbines, power plants, spacecraft, cooling of nuclear reactors, etc. Mahabaleshwar et al. [31] discussed the radiation impact on the flow of Casson nanofluid across a shrinking/stretching sheet along with the characteristic of mass transpiration. Their results proved that the temperature rapidly increases due to the radiation effect. Goud Bejawada et al. [32] explored the substance reaction effect on the radiative flow of magnetized Casson liquid through a tending irregular sheet in a porous medium. They observed that the temperature declines in the presence of the Forchheimer porous factor and the radiation factor. Swain et al. [33] investigated the steady buoyancy flow near a stagnation point by incorporating the

special third-grade fluid past a moving sheet with radiation and suction effects. They obtained multiple solutions in the case of opposing flows only. Their results also revealed that temperature is a growing function of the thermal radiation effect. The effects of the heat sink and heat source on the MHD flow of Casson fluid across a porous shrinking sheet with radiation effect were inspected by Swain et al. [34]. Their explorations suggested that the range of multiple outcomes is enhanced due to magnetic, suction, and Casson parameters. Recently, Adilakshmi et al. [35] analyzed the 2D flow of Sisko fluid past an irregular stretchable sheet with radiation and magnetic effects. Their findings revealed that the velocity augments owing to the Sisko liquid factor, whilst the concentration and temperature declined.

After carefully reviewing the previous work and taking motivation from the physical aspects of the cobalt nanoparticles. The current work considers the time-dependent flow of second-grade fluid towards the stagnation point by incorporating cobalt nanoparticles along with Joule heating, convective boundary conditions, and magnetic effects. The main purpose is to select an appropriate transformation to change the leading flow equations into a similarity system of ordinary differential equations. Then this system is solved by employing a bvp4c solver to get dual solutions as well as the data set, which is utilized for testing, training, and validation through advanced machine learning. Also, the performance of the model for the distinct statistical methods is inspected through advanced machine learning. The stability analysis is also performed to discover the stable solution. In this research, the following queries are answered.

- What kind of impact on the critical values for different parameters, such as the magnetic, Biot number, and suction parameters?
- Have any significant influence of the Biot number, Eckert number, and radiation factor on the temperature distribution?
- What kind of changes occur in the velocity and temperature fields by varying the second-grade parameter?
- In the case of multiple solutions, which solution is practically acceptable?
- What is the impact of different physical factors using advanced machine learning?

This type of flow problem has not been investigated earlier to the best of our knowledge, thus the solutions are significant and novel. The special second-grade fluid is utilized as a non-Newtonian liquid, and its outcomes can be utilized as a benchmark for potential exploration of other non-Newtonian liquids.

2 Framework of Flow Model

The two-dimensional unsteady stagnation-point nanofluid and heat transfer characteristic flow via incorporating a second-grade (non-Newtonian) model in the region $y_d > 0$ established through a permeable movable sheet with Lorentz forces is studied. In addition, the impact of the thermal radiation, Joule heating, and convective boundary conditions are also considered. Fig. 1 exemplifies the flow configuration of the nanofluid problem in terms of the Cartesian coordinate (x_d, y_d), where x_d and y_d axes run along the horizontal and perpendicular surface of the sheet, respectively. Moreover, the radiative heat flux is expressed as $q_{rad} = -\left(16\sigma^* T_\infty^3/3k^*\right)\partial T_d/\partial y_d$, in which the corresponding symbols called the Stefan-Boltzmann σ^* and k^* the mean absorption. In the present work, the requisite nanofluid is proposed by $CoFe_2O_4$ nanoparticles and the convectional liquid (H_2O). Suppose that the variable velocities of the fluid at the wall surface and far-field free stream surface of the sheet are denoted by $u_{wd}(x_d, t_d)$ and $u_{ed}(x_d, t_d)$, respectively. Additionally, the suction/injection or mass flux velocity is represented by $v_{wd}(t_d)$. It is further assumed that the sheet surface is heated by convection

from a hot fluid at a variable temperature T_{wdf} that provides the heat transfer coefficient h_f, while T_∞ indicates the temperature far away from the sheet. As suggested by Fosdick and Rajagopal [36], the Cauchy stress describes for the general second-grade fluid as:

$$T_h = -p_s \mathbf{I}_s + \mu A_s + \gamma_c A_t + \gamma_d A_s^2 \tag{1}$$

where p_s denotes the pressure, $\mu \geq 0$ the dynamic viscosity, $\mathbf{I}_s$ is the identity tensor, γ_d and γ_c designate to normal stresses with $\gamma_c \geq 0$ and $\gamma_d + \gamma_c = 0$, while A_s and A_t indicate the Rivlin-Ericksen tensors and are described as:

$$A_s \equiv (\text{grad}\mathbf{V})^T + \text{grad}\mathbf{V}, A_t \equiv \frac{dA_s}{dt_d} + A_s\left[\text{grad}\mathbf{V} + (\text{grad}\mathbf{V})^T\right] \tag{2}$$

where $\frac{d}{dt_d}$ shows the total or material derivative and $\mathbf{V}$ means the fluid velocity. The current research scrutinizes a special kind of second-grade fluid where γ_d is of the order of δ_d^3, in which δ_d denotes the boundary layer width. Moreover, the constant magnetic effect B_0 is directed upright to the sheet. Using the aforesaid assumptions along with the boundary layer scaling, the leading governing equations in the context of PDEs are expressed as (Roy and Pop [37]):

$$\frac{\partial u_d}{\partial x_d} + \frac{\partial v_d}{\partial y_d} = 0 \tag{3}$$

$$\frac{\partial u_d}{\partial t_d} + u_d\frac{\partial u_d}{\partial x_d} + v_d\frac{\partial u_d}{\partial y_d} - \frac{\partial u_{ed}}{\partial t_d} - u_{ed}\frac{\partial u_{ed}}{\partial x_d} = \frac{\mu_{nf}}{\rho_{nf}}\frac{\partial^2 u_d}{\partial y_d^2} + 2\frac{\gamma_d}{\rho_{nf}}\frac{\partial u_d}{\partial y_d}\frac{\partial^2 u_d}{\partial x_d \partial y_d} - \frac{\sigma_{nf}}{\rho_{nf}}B_0^2\left(u_d - u_{ed}\right), \tag{4}$$

$$\frac{\partial T_d}{\partial t_d} + u_d\frac{\partial T_d}{\partial x_d} + v_d\frac{\partial T_d}{\partial y_d} = \frac{k_{nf}}{\left(\rho c_p\right)_{nf}}\frac{\partial^2 T_d}{\partial y_d^2} + \frac{16\sigma^* T_\infty^3}{3k^*\left(\rho c_p\right)_{nf}}\frac{\partial^2 T_d}{\partial y_d^2} + \frac{\sigma_{nf}}{\left(\rho c_p\right)_{nf}}B_0^2\left(u_d - u_{ed}\right)^2, \tag{5}$$

with initial and boundary conditions (IBCs) are

$$\begin{aligned} &t_d < 0\colon u_d = 0, v_d = 0, T_d = T_\infty \text{for all } x_d \text{ and } y_d,\\ &t_d \geq 0\colon u_d = u_{wd}\left(x_d, t_d\right) = \tfrac{cx_d}{1-\gamma e t_d}, v_d = v_{wd}\left(t_d\right), -k_{nf}\tfrac{\partial T_d}{\partial y_d} = h_f\left(T_{wdf} - T_d\right) \text{ at } y_d = 0,\\ &u_d \to u_{ed}\left(x_d, t_d\right) \to \tfrac{dx_d}{1-\gamma e t_d}, T_d \to T_\infty \text{ as } y_d \to \infty. \end{aligned} \tag{6}$$

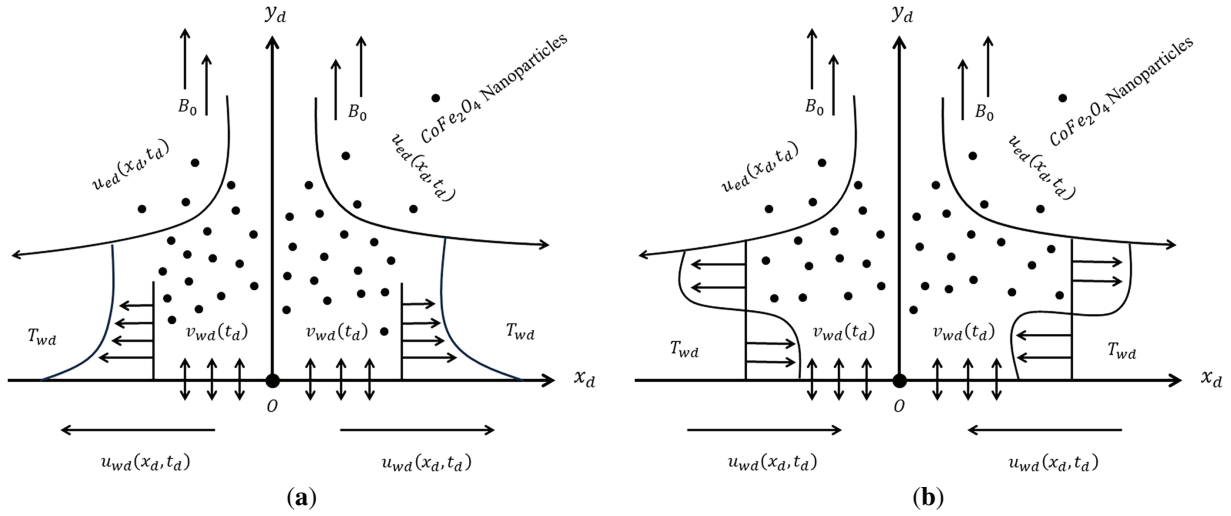

Figure 1: Physical sketch of the fluid flow for (a) the stretching sheet and (b) the shrinking sheet problem

In governing equations above, T_d denotes the temperature of the nanofluid, and u_d, v_d indicate the components of the velocity in x_d-axis and y_d-axis, respectively. Moreover, γ_e represents the unsteady factor having dimension $(\text{time})^{-1}$, while d the strain-rate parameter. However, $c < 0$ is used for the shrinkable sheet and $c > 0$ for stretchable sheet. Finally, the variable wall temperature is expressed by $T_{wdf} = T_\infty + T_r \left(\frac{x_d}{l_d}\right)^2$, where T_r is the reference temperature and l_d is the characteristic length.

Additionally, the remaining mathematical notations in the governing equations above represent the TPPs (thermophysical properties) of the nanofluid and their equivalent correlations are listed in Table 1.

Here, φ_{np} signifies the solid nanoparticles volume fraction but the particular value $\varphi_{np} = 0$ characterizes the common (regular) base fluid. Moreover, the subscript f specify the regular liquid, np nanoparticles, and nf for nanofluid. Although, c_p corresponds to the specific heat at consistent pressure. Table 2 shows the thermophysical values $CoFe_2O_4$ nanoparticles with the regular fluid.

Table 1: The TPPs correlations of the ($CoFe_2O_4$/water) nanofluid

Properties	Correlations
Dynamic viscosity	$\mu_{nf} = \mu_f \left(1 - \varphi_{np}\right)^{-2.5}$
Heat capacity	$\left(\rho c_p\right)_{nf} = \left(\rho c_p\right)_f \left[\varphi_{np}\left(\frac{\left(\rho c_p\right)_{np}}{\left(\rho c_p\right)_f}\right) + \left(1 - \varphi_{np}\right)\right]$
Density	$\rho_{nf} = \rho_f \left[\varphi_{np}\left(\frac{\rho_{np}}{\rho_f}\right) + \left(1 - \varphi_{np}\right)\right]$
Thermal conductivity	$k_{nf} = k_f \left[\frac{\left(k_{np} + 2k_f\right) - 2\varphi_{np}\left(k_f - k_{np}\right)}{\left(k_{np} + 2k_f\right) + \varphi_{np}\left(k_f - k_{np}\right)}\right]$
Electrical conductivity	$\sigma_{nf} = \sigma_f \left[1 + \frac{3\left(\frac{\sigma_{np}}{\sigma_f} - 1\right)}{\left(\frac{\sigma_{np}}{\sigma_f} + 2\right) - \left(\frac{\sigma_{np}}{\sigma_f} - 1\right)\varphi_{np}}\right]$

Table 2: The experimental data of ($CoFe_2O_4$/water) nanofluid

Properties	$\rho\ (\text{kg/m}^3)$	k (W/mK)	c_p (J kg K)	σ (S/m)	Pr
$CoFe_2O_4$	4907	3.7	700	5.51×10^9	—
H_2O	997.1	0.613	4179	5.5×10^{-6}	6.2

For further simplicity of the flow problem, the similarity variables are introduced as follows:

$$\psi = \left(\frac{d\upsilon_f}{1 - \gamma_e t_d}\right)^{1/2} x_d G\left(\xi\right), \ \xi = y_d \left(\frac{d}{\upsilon_f \left(1 - \gamma_e t_d\right)}\right)^{1/2}, \ S\left(\xi\right) = \frac{T_d - T_\infty}{T_{wdf} - T_\infty}, \tag{7}$$

which identically satisfied the continuity Eq. (3) and ξ signifies the pseudo-similarity constraint. For the similarity solutions, it is necessary to express $h_f = h_f^* (1-\gamma_e t_d)^{-1/2}$, $\gamma_d = \gamma_{d0}(1-\gamma_e t_d)$, and $\sigma_f = \sigma_f^*/1-\gamma_e t_d$, where h_f^* is the uniform heat transfer, γ_{d0} and σ_f^* correspond to the electrical conductivity of H_2O and arbitrary constant, respectively. In addition, substituting Eq. (7) into Eqs. (4) and (5) yields:

$$\frac{\mu_{nf}/\mu_f}{\rho_{nf}/\rho_f} G''' + \frac{2K_d}{\rho_{nf}/\rho_f} G''^2 + GG'' - G'^2 + \beta_d \left(1 - G' - \frac{\xi}{2} G''\right) + 1 + \frac{\sigma_{nf}/\sigma_f}{\rho_{nf}/\rho_f} M_d (1-G') = 0, \tag{8}$$

$$\left(\frac{k_{nf}}{k_f} + \frac{4}{3} R_{radd}\right) S'' + \Pr \frac{(\rho c_p)_{nf}}{(\rho c_p)_f} \left(GS' - 2SG' - \beta_d \frac{\xi}{2} S'\right) + \Pr \frac{\sigma_{nf}}{\sigma_f} Ec_d M_d (1-G')^2 = 0, \tag{9}$$

where $\beta_d = \gamma_e/d$ the unsteadiness factor, $R_{radd} = 4\sigma^* T_\infty^3/k^* k_f$ the radiation parameter, $\Pr = \alpha_f/\upsilon_f$ the Prandtl number, $Bi_d = \dfrac{h_f^*}{k_f}\sqrt{\dfrac{\upsilon_f}{d}}$ the Biot number, $K_d = \gamma_{d0} d/\mu_f$ signifies the viscosity factor, $Ec_d = \dfrac{d^2 l_d^2/(1-\gamma_e t_d)^2}{(c_p)_f T_r} = \dfrac{u_{ed}^2 (l_d)}{(c_p)_f T_r}$ the Eckert number, and $M_d = \sigma_f^* B_0^2/\rho_f d$ the magnetic parameter.

The transformed boundary conditions are

$$\begin{aligned} &G(\xi) = f_{wd},\ G'(\xi) = \lambda_d,\ \tfrac{k_{nf}}{k_f} S'(\xi) = -Bi_d (1 - S(\xi)) \ \text{ at } \xi = 0, \\ &G'(\xi) \to 1, S(\xi) \to 0, \ \text{ as } \xi \to \infty, \end{aligned} \tag{10}$$

where $\lambda_d = c/d$ is the moving parameter, and f_{wd} represents the mass velocity transpiration. Also, $f_{wd} > 0$ is used for suction and $f_{wd} < 0$ for injection.

The quantities of engineering interest like the skin friction C_f and the Nusselt number Nu_{x_d}, which are characterized as follows:

$$C_f = \frac{1}{\rho_f u_{ed}^2} \left(\mu_{nf} \frac{\partial u_d}{\partial y_d}\right)_{y_d=0}, \text{ and } Nu_{x_d} = \frac{x_d}{k_f (T_{wdf} - T_\infty)} \left(-k_{nf} \left(\frac{\partial T_d}{\partial y_d}\right)\Big|_{y_d=0} + q_{rad}|_{y_d=0}\right). \tag{11}$$

Putting Eqs. (7) in (11) yields

$$\mathrm{Re}_{x_d}^{1/2} C_f = \frac{\mu_{nf}}{\mu_f} G''(0), \text{ and } \mathrm{Re}_{x_d}^{-1/2} Nu_{x_d} = -\left(\frac{k_{nf}}{k_f} + \frac{4}{3} R_{radd}\right) S'(0), \tag{12}$$

where $\mathrm{Re}_{x_d} = \dfrac{u_{ed} x_d}{\upsilon_f}$ signifies the local Reynolds number.

3 Stability Analysis of Solutions

In order to perform a stability analysis of the solutions, we need to consider the unsteady problem [33,34]. Eq. (3) still holds, while Eqs. (4) and (5) of our existing problem are already in unsteady form and therefore there is no need to repeat and rewrite the same equations again in this portion of the work. Therefore, to perform the working calculation procedure for the stability analysis of the solutions, the following transformations are introduced:

$$\psi = \left(\frac{d\upsilon_f}{1-\gamma_e t_d}\right)^{1/2} x_d G(\xi, \tau_{sd}), \ \xi = y_d \left(\frac{d}{\upsilon_f (1-\gamma_e t_d)}\right)^{1/2}, \ S(\xi, \tau_{sd}) = \frac{T_d - T_\infty}{T_{wdf} - T_\infty}, \ \tau_{sd} = \frac{dt_d}{(1-\gamma_e t_d)}, \tag{13}$$

where τ_{sd} is the new dimensionless time. Using Eq. (13) in Eqs. (4) and (5) yields:

$$\frac{\mu_{nf}/\mu_f}{\rho_{nf}/\rho_f}\frac{\partial^3 G}{\partial \xi^3}+\frac{2K_d}{\rho_{nf}/\rho_f}\left(\frac{\partial^2 G}{\partial \xi^2}\right)^2+G\frac{\partial^2 G}{\partial \xi^2}-\left(\frac{\partial G}{\partial \xi}\right)^2+\beta_d\left(1-\frac{\partial G}{\partial \xi}-\frac{\xi}{2}\frac{\partial^2 G}{\partial \xi^2}\right)$$
$$+\frac{\sigma_{nf}/\sigma_f}{\rho_{nf}/\rho_f}M_d\left(1-\frac{\partial G}{\partial \xi}\right)+1-(1+\beta_d\tau_{sd})\frac{\partial^2 G}{\partial \xi\,\partial \tau_{sd}}=0, \tag{14}$$

$$\frac{1}{\Pr\dfrac{(\rho c_p)_{nf}}{(\rho c_p)_f}}\left(\frac{k_{nf}}{k_f}+\frac{4}{3}R_{radd}\right)\frac{\partial^2 S}{\partial \xi^2}+G\frac{\partial S}{\partial \xi}-2S\frac{\partial G}{\partial \xi}-\beta_d\frac{\xi}{2}\frac{\partial S}{\partial \xi}$$
$$+\frac{\dfrac{\sigma_{nf}}{\sigma_f}}{\dfrac{(\rho c_p)_{nf}}{(\rho c_p)_f}}Ec_d M_d\left(1-\frac{\partial G}{\partial \xi}\right)^2-(1+\beta_d\tau_{sd})\frac{\partial S}{\partial \tau_{sd}}=0, \tag{15}$$

and are subject to the BCs are

$$G(0,\tau_{sd})=f_{wd},\ \frac{\partial G}{\partial \xi}(0,\tau_{sd})=\lambda_d,\ \frac{k_{nf}}{k_f}\frac{\partial S}{\partial \xi}(0,\tau_{sd})=-Bi_d\,(1-S(0,\tau_{sd}))\ ,$$
$$\frac{\partial G}{\partial \xi}(\xi,\tau_{sd})\to 1, S(\xi,\tau_{sd})\to 0,\ \text{ as } \xi\to\infty. \tag{16}$$

To test the stability of the steady flow solution $G(\xi)=G_0(\xi)$ and $S(\xi)=S_0(\xi)$ satisfying the boundary value problem (3)–(6), and we write the following perturbations [33,34].

$$G(\xi,\tau_{sd})=G_0(\xi)+e^{-\Sigma_d\tau_{sd}}g(\xi,\tau_{sd}),\ S(\xi,\tau_{sd})=S_0(\xi)+e^{-\Sigma_d\tau_{sd}}s(\xi,\tau_{sd}), \tag{17}$$

where $g(\xi,\tau_{sd})$ and $s(\xi,\tau_{sd})$ functions correspond the small relative to $G_0(\xi)$ and $S_0(\xi)$, respectively, and Σ_d denotes the eigenvalue. The set of infinite eigenvalues $\Sigma_{d_1}<\Sigma_{d_2}<\Sigma_{d_3}\ldots$ are obtained from the Eqs. (14)–(16). There is an initial decay and growth of disturbances; if the smallest eigenvalues are positive or negative then the flow becomes stable or unstable, respectively. Substituting Eq. (17) into Eqs. (14) and (15), one obtains the following linearized problem:

$$\frac{\mu_{nf}/\mu_f}{\rho_{nf}/\rho_f}\frac{\partial^3 g}{\partial \xi^3}+\frac{4K_d}{\rho_{nf}/\rho_f}G_0''\frac{\partial^2 g}{\partial \xi^2}+G_0\frac{\partial^2 g}{\partial \xi^2}+G_0''g-2G_0'\frac{\partial g}{\partial \xi}-\beta_d\left(\frac{\partial g}{\partial \xi}+\frac{\xi}{2}\frac{\partial^2 g}{\partial \xi^2}\right)$$
$$-\frac{\sigma_{nf}/\sigma_f}{\rho_{nf}/\rho_f}M_d\frac{\partial g}{\partial \xi}+(1+\beta_d\tau_{sd})\left(\Sigma_d\frac{\partial g}{\partial \xi}-\frac{\partial^2 g}{\partial \xi\,\partial \tau_{sd}}\right)=0, \tag{18}$$

$$\frac{1}{\Pr\dfrac{(\rho c_p)_{nf}}{(\rho c_p)_f}}\left(\frac{k_{nf}}{k_f}+\frac{4}{3}R_{radd}\right)\frac{\partial^2 s}{\partial \xi^2}+G_0\frac{\partial s}{\partial \xi}+S_0'g-2S_0\frac{\partial g}{\partial \xi}-2G_0's-\beta_d\frac{\xi}{2}\frac{\partial s}{\partial \xi}$$
$$+\frac{\dfrac{\sigma_{nf}}{\sigma_f}}{\dfrac{(\rho c_p)_{nf}}{(\rho c_p)_f}}Ec_d M_d\left(2G_0'\frac{\partial g}{\partial \xi}-2\frac{\partial g}{\partial \xi}\right)+(1+\beta_d\tau_{sd})\left(\Sigma_d s-\frac{\partial s}{\partial \tau_{sd}}\right)=0, \tag{19}$$

and are subject to the BCs are

$$g(0,\tau_{sd})=0,\ \frac{\partial g}{\partial \xi}(0,\tau_{sd})=0,\ \frac{k_{nf}}{k_f}\frac{\partial s}{\partial \xi}(0,\tau_{sd})=Bi_d s(0,\tau_{sd}),$$
$$\frac{\partial g}{\partial \xi}(\xi,\tau_{sd})\to 0,\ s(\xi,\tau_{sd})\to 0,\ \text{ as } \xi\to\infty. \tag{20}$$

By inserting $\tau_{sd}=0$, the solutions $G(\xi)=G_0(\xi)$ and $S(\xi)=S_0(\xi)$ of the steady state Eqs. (8) and (9) are obtained. In Eqs. (18) and (19), the initial decay or growth of the solution in Eq. (17) are denoted by the functions $g=g_0(\xi)$ and $s=s_0(\xi)$. Due to this respect, we need to crack the linear eigenvalue problem:

$$\frac{\mu_{nf}/\mu_f}{\rho_{nf}/\rho_f}g_0'''+\frac{4K_d}{\rho_{nf}/\rho_f}G_0''g_0''+G_0g_0''+G_0''g_0-2G_0'g_0'-\beta_d\left(g_0'+\frac{\xi}{2}g_0''\right)$$
$$-\frac{\sigma_{nf}/\sigma_f}{\rho_{nf}/\rho_f}M_d g_0'+\Sigma_d g_0'=0, \tag{21}$$

$$\frac{1}{\Pr\dfrac{(\rho c_p)_{nf}}{(\rho c_p)_f}}\left(\frac{k_{nf}}{k_f}+\frac{4}{3}R_{radd}\right)s_0''+G_0s_0'+S_0'g_0-2S_0g_0'-2G_0's_0-\beta_d\frac{\xi}{2}s_0'$$
$$+\frac{\dfrac{\sigma_{nf}}{\sigma_f}}{\dfrac{(\rho c_p)_{nf}}{(\rho c_p)_f}}Ec_dM_d\left(2G_0'g_0'-2g_0'\right)+\Sigma_d s_0=0, \tag{22}$$

and are subject to the BCs are

$$g_0(0)=0,\ g_0'(0)=0,\ \frac{k_{nf}}{k_f}s_0'(0)=Bi_d s_0(0),$$
$$g_0'(\xi)\to 0,\ s_0(\xi)\to 0,\ \text{ as } \xi\to\infty. \tag{23}$$

In order to solve this problem, a non-homogeneous boundary conditions needs to be considered. As it has been suggested by Haris et al. [38], the range of possible eigenvalues can be determined by relaxing a boundary condition on $g_0'(\xi)$ and $s_0(\xi)$. Therefore, we relax the condition that $g_0'(\xi)\to 0$ as $\xi\to\infty$. In addition, for a fixed value of Σ_d, we solve the system of Eqs. (21)–(23) with a new boundary condition $g_0''(0)=1$.

4 Methodology

The system of similarity ODE Eqs. (8) and (9) in conjunction with the boundary conditions (10) are solved numerically using bvp4c. A program in MATLAB is used by the set of equations that researchers commonly utilize to solve boundary value problems (BVPs). This present scheme relies on the finite difference technique, uses a formula like Lobatto IIIa collocation to get a C^1-continuous outcome. The fundamental source of this IIIa-step Lobatto formula is the disturbed collocation process, generally acknowledged as the Runge-Kutta technique. The bvp4c solver is employed for the collocation method, which gives accuracy and fourth grade precision.

To change the highly nonlinear ODEs into the first-order by introducing new. The following are new variables:

$$G = H_a, G' = H_b, G'' = H_c, S = H_d, S' = H_e \tag{24}$$

Now substituting Eq. (24) into the Eqs. (8) and (9), we get the following set of equations.

$$\frac{d}{d\xi}\begin{pmatrix} H_a \\ H_b \\ H_c \\ H_d \\ H_e \end{pmatrix} = \begin{pmatrix} H_b \\ H_c \\ \frac{\rho_{nf}/\rho_f}{\mu_{nf}/\mu_f}\left(-\frac{2K_d}{\rho_{nf}/\rho_f}H_c^2 - H_aH_c + H_b^2 - \beta_d\left(1 - H_b - \frac{\xi}{2}H_c\right) - 1 - \frac{\sigma_{nf}/\sigma_f}{\rho_{nf}/\rho_f}M_d\left(1 - H_b\right)\right) \\ H_e \\ \frac{1}{\left(\frac{k_{nf}}{k_f} + \frac{4}{3}R_{radd}\right)}\left(-\Pr\frac{(\rho c_p)_{nf}}{(\rho c_p)_f}\left(H_aH_e - 2H_bH_d - \beta_d\frac{\xi}{2}H_e\right) - \Pr\frac{\sigma_{nf}}{\sigma_f}Ec_dM_d\left(1 - H_b\right)^2\right) \end{pmatrix} \tag{25}$$

To tackle the above equation, the unknown and known initial boundary conditions are considered:

$$H_a(0) = f_{wd}, H_b(0) = \lambda_d, H_c(0) = N_B, \frac{k_{nf}}{k_f}H_e(0) = -Bi_d\left(1 - H_d(0)\right), H_e(0) = N_C. \tag{26}$$

In addition, the approximate constants N_C and N_B are meant to utilize the suitable useful shooting method in a such a way that continuously predates calculations through bvp4c satisfy the following boundary constraints:

$$H_b(\xi) \to 1, H_d(\xi) \to 0, \text{ as } \xi \to \infty. \tag{27}$$

Thus, the guess or estimate for the upper branch (UB) solution is simple and clear as associate to the estimate picking for the lower branch (LB) solution. For the LB, it is relatively complex to choose a suitable estimate; as a result, one is picking the estimate keeping in a mind that the Eq. (27) holds asymptotically as well as the objective of precision and accuracy corresponding to 10^{-10}.

5 Results and Discussion

The accuracy, authenticity, and precision has been shown by comparing our results with available results of Bhattacharyya [39] in the limited cases which has been depicted graphically in Fig. 2 and observed in a tremendous agreement. In addition, it can be seen that the outcomes in both branches agreed very well. This gives us confidence that the scheme is correct and can be used to obtain results that are not yet available.

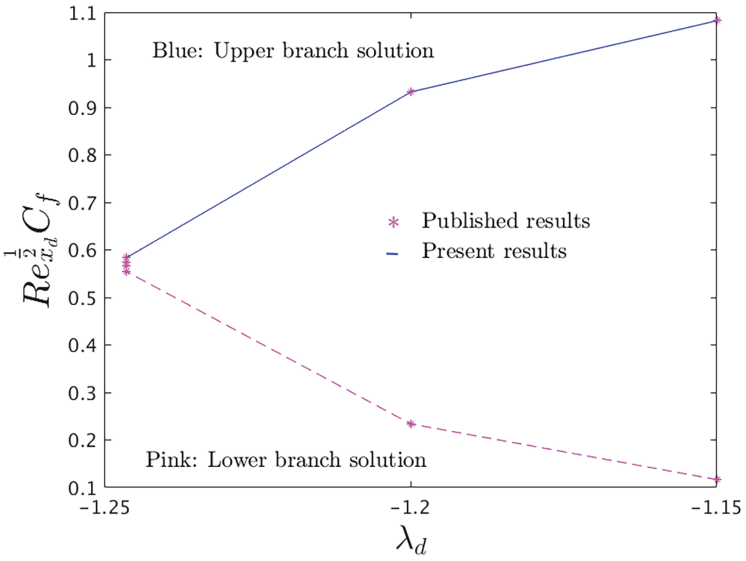

Figure 2: A comparison of the skin friction coefficient vs. the shrinking parameter due to the absence of other physical influential parameters

Interpretation of the Results

To simulate the proposed problem, the controlling parameters are considered as $\varphi_{np} = 0.030$, $K_d = 0.5$, $f_{wd} = 1.6$, $\beta_d = -2.0$, $\lambda_d = -2.5$, $M_d = 0.1$, $Bi_d = 0.5$, $Ec_d = 0.5$, and $R_{radd} = 2.0$. Tables 3 and 4 show the results of the skin friction (SF) and the local Nusselt number (LNN) for UB solution and LB solution by involving the various notable parameters. Solutions are revealed that the LNN enhances for UB solution and shrinks for LB solution in the presence of φ_{np}, whilst the SF behaves a gradually upper in dual outcomes. In other words, the LNN augmented by 1.50% for the UB solution and reduced by 0.65% because of the greater values of φ_{np}. Additionally, the SF intensifies for the UB solution and delay for the LB solution due to the superior influence of K_d and M_d. Conversely, the larger influence of Bi_d enhances the LNN in both outcomes. With consecutive alteration in the values of Bi_d, the LNN enhances by 22.65% for the UB solution and 11.75% for the LB solution.

Table 3: Numerical outcomes of the skin friction for the different parameters when $f_{wd} = 1.6$, $\beta_d = -2.0$, $\lambda_d = -1.5$, Pr = 6.2, $R_{radd} = 2.0$, $Ec_d = 0.5$, and $Bi_d = 0.5$

φ_{np}	K_d	M_d	Skin Friction Coefficient	
			UB Solution	LB Solution
0.022	0.5	0.1	20.080951	−4.0634015
0.026	–	–	20.167460	−4.1329310
0.030	–	–	20.253186	−4.2028131
0.022	0.1	0.1	4.6959236	−2.9601355
–	0.2	–	6.9501355	−3.8797345
–	0.3	–	9.9677712	−4.3639514

(Continued)

Table 3 (continued)

φ_{np}	K_d	M_d	Skin Friction Coefficient	
			UB Solution	LB Solution
0.022	0.5	0.3	21.156525	−4.0782330
–	–	0.4	21.413624	−4.0409555
–	–	0.5	21.666651	−4.0013746

Table 4: Numerical outcomes of the Nusselt number for the different factors when $f_{wd} = 1.6$, $\beta_d = -2.0$, $\lambda_d = -1.5$, $\mathrm{Pr} = 6.2$, $K_d = 0.5$, $Ec_d = 0.5$, $R_{radd} = 2.0$, and $M_d = 0.1$

φ_{np}	Bi_d	Nusselt Number	
		UB solution	LB solution
0.022	0.50	1.3825998	3.1417583
0.026	–	1.3918740	3.0770020
0.030	–	1.4011738	2.9671357
0.022	0.20	0.6033329	2.3010766
–	0.30	0.8783728	2.7028783
–	0.40	1.1376919	2.9614346

The SF and the LNN in the presence of water-based $CoFe_2O_4$ vs. β_d for the UB and LB solutions with changing values of f_{wd} are epitomized in Figs. 3 and 4, respectively. The SF upsurges and the LNN reduces because of the climb in the unsteadiness parameter (decelerating shrinking sheet) $\beta_d \leq 0$. The portraits demonstrate that the skin friction boosts in the case of the UBS and shrinkages in the case of lower branch solution with superior values of f_{wd} whereas the Nusselt number declines for both solutions. Also, multiple outcomes are presented for each chosen value of f_{wd} against β_d, where UB result and LB result are indicated through a solid blue and dashed pink lines, respectively. The two different solutions survive for a certain point, whereas no solution exists beyond this point. The critical point where the solution is unique is signified by the solid ball in both portraits. It is noted that the critical points vs. the unsteady factor are far away always in the particular area, as a result, the solitary critical point is obtainable for $f_{wd} = 0.2$. Moreover, these points are so isolated in the negative area which ultimately stopped the calculations at $\beta_d = -3.0$ for the choices of ($f_{wd} = 0.4$ and 0.6).

Figs. 5 and 6 demonstrate the behavior of the SF and the LNN vs. λ_d for the UB and LB solutions with the varied values of f_{wd}, respectively. It is noted from the graphs that the SF augments and shrinks for the UB solution and LB solution owing to the superior impact of f_{wd} but the LNN constantly enhances in the LB outcome and reduces for the UB outcome. Also, the black solid balls in both portraits symbolize the bifurcation point at which the UB solution and LB solution connect jointly and mathematically demonstrated as $\lambda_d C$. The computational values of different $f_{wd} = 0.2$, 0.4 and 0.6 are signified as −2.2410, −2.7037, and −3.3987, respectively. The absolute of the critical points is elevated due to the greater impact of f_{wd}. Therefore, the trailing in the boundary layer separation is happened due to the larger values of f_{wd}. In addition, an growing the suction factor consequences in the creation of multiple outcomes across a bigger choice of the velocity ratio factor. The aforesaid

character is accurate due to the augment in the suction factor which ultimately causes in a superior velocity of the flow close to the wall.

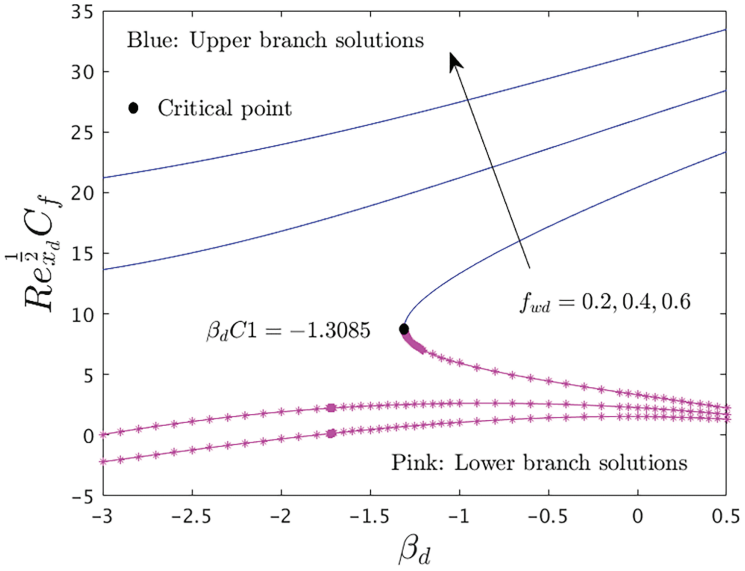

Figure 3: The skin friction against β_d for different values of f_{wd}

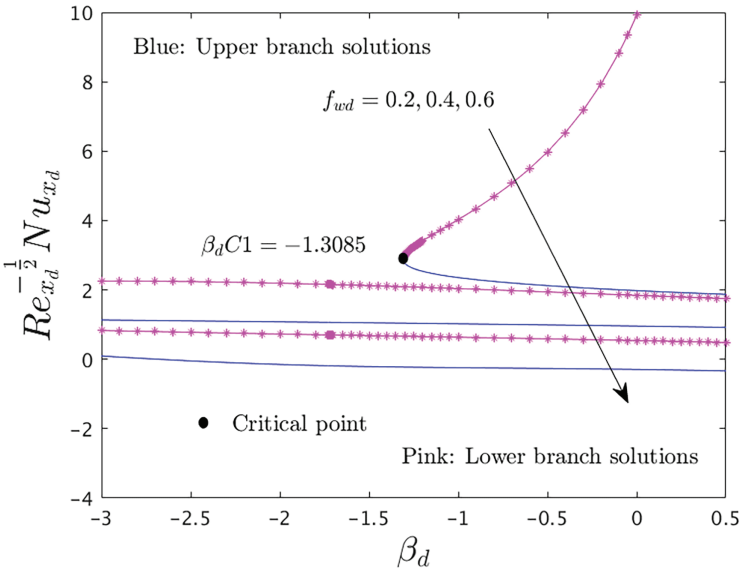

Figure 4: The Nusselt number against β_d for different values of f_{wd}

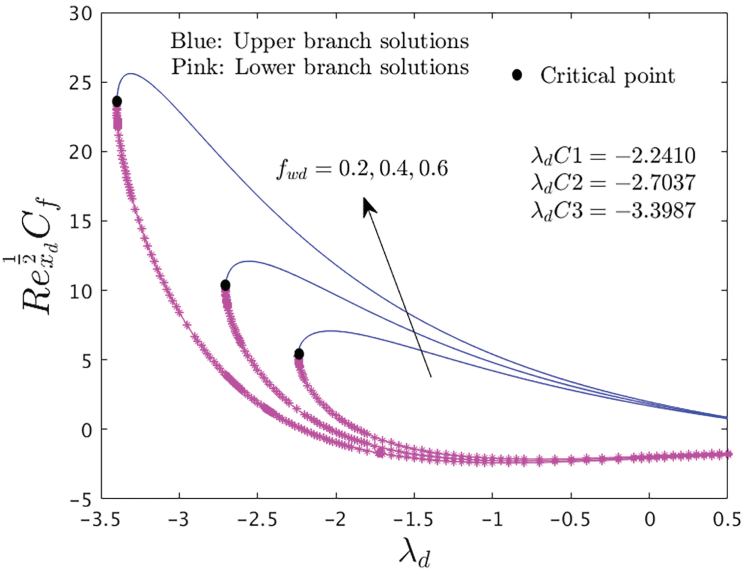

Figure 5: The SF vs. λ_d for different f_{wd}

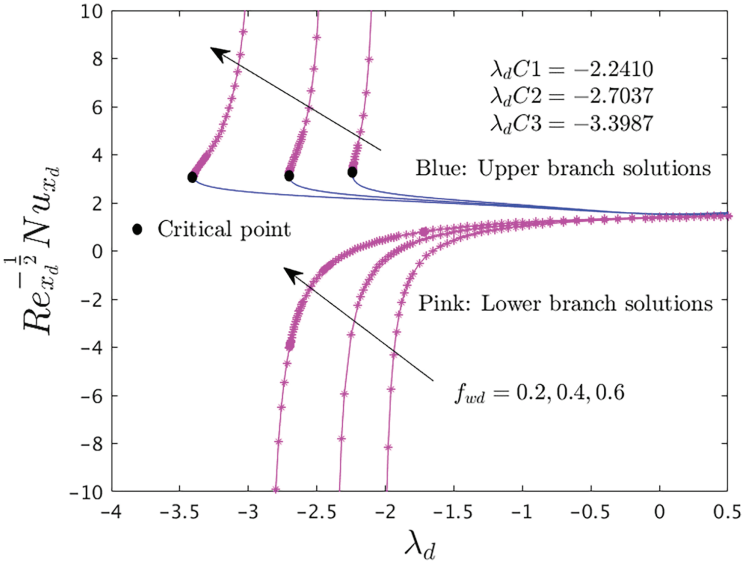

Figure 6: The LNN vs. λ_d for different f_{wd}

Figs. 7 and 8 illustrate the influence of K_d on the velocity and temperature distribution vs. ξ for both solutions, respectively. The results suggest that the velocity declines frequently for the LB solution and then unexpectedly strengthens for the UB solution with increasing values of K_d. In addition, the temperature grows for the LB solution and shrinks for UB solution due to greater values of K_d. Thus, the thermal and the momentum boundary layer thicknesses dramatically moderate due to K_d. This argument makes sense as the adjacent particles must travel faster due to the greater normal tension forces.

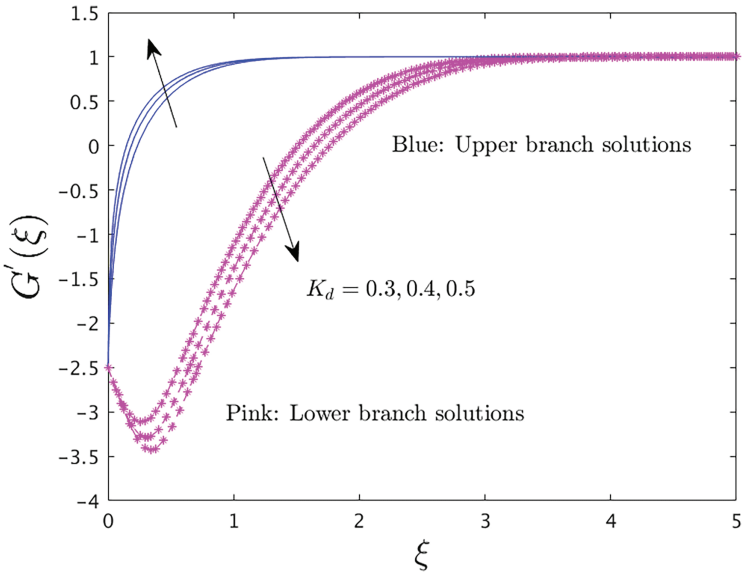

Figure 7: The velocity profile for different K_d

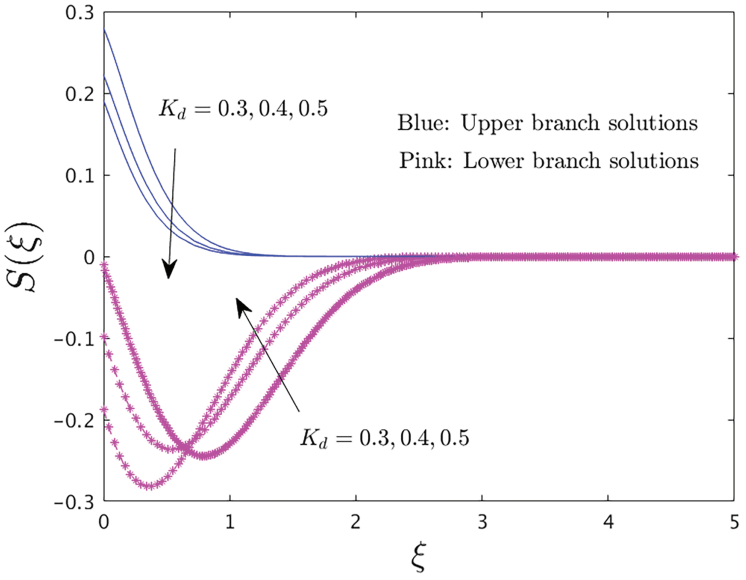

Figure 8: The temperature profile for different K_d

Figs. 9 and 10 demonstrate the influence of the magnetic factor M_d on the fluid velocity and temperature distribution of water-based $CoFe_2O_4$ for both solutions. The outcomes disclose that the velocity enhances significantly for the LB outcome and declines for the UB outcome due to higher values of M_d. But, the contradictory trend is observed for the temperature distribution because of M_d. Thus, the greater magnetic parameter guides to a noteworthy contraction in the thermal and momentum boundary layers.

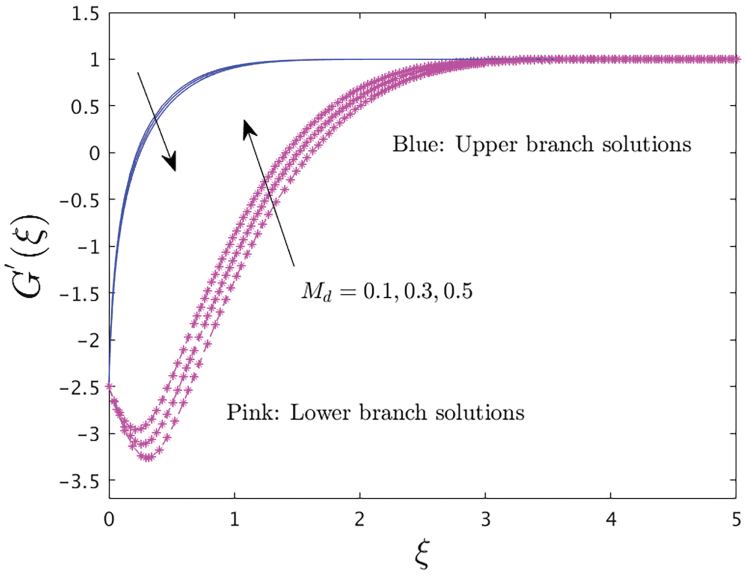

Figure 9: The velocity profile for different M_d

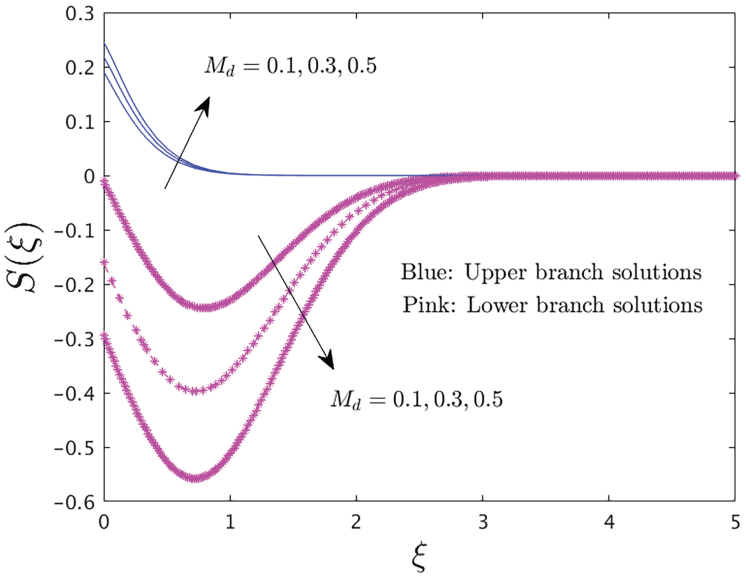

Figure 10: The temperature profile for different M_d

The impact of Ec_d on the temperature distribution for both solutions is depicted in Fig. 11. It is seen that the temperature distribution increases for the UB solutions and decreases for the LB solutions due to increasing values of Ec_d. In addition, both solutions are satisfied the boundary conditions asymptotically. Moreover, the impact of Ec_d is better in the case of LB solution compared to UB solution.

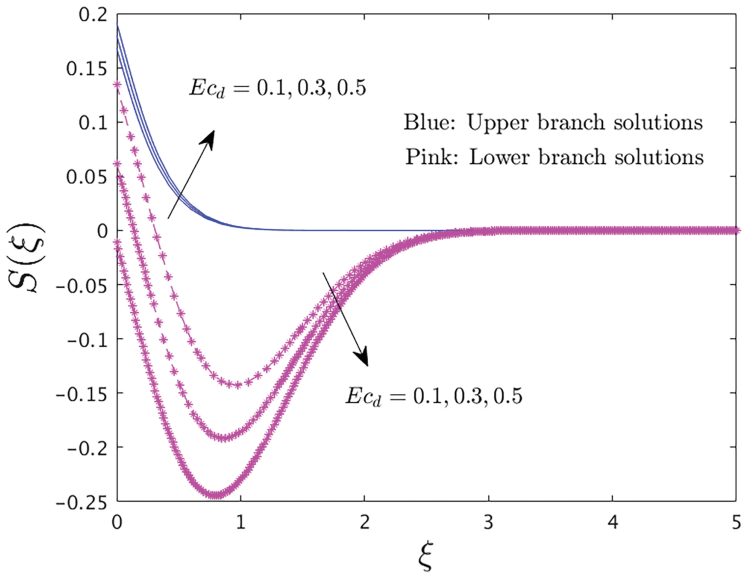

Figure 11: The temperature distribution for different Ec_d

Table 5 shows the distinct numerical eigenvalues Σ_d for the several change values of β_d when $f_{wd} = 0.2$, $M_d = 0.1$, $\lambda_d = -2.5$, $K_d = 0.5$, $\varphi_{np} = 0.03$, $\mathrm{Pr} = 6.2$, $R_{radd} = 2.0$, $Ec_d = 0.5$, and $Bi_d = 0.5$. From the tabulated values and Eq. (17), it is evident that negative eigenvalues lead to an initial growth of disturbances; therefore, the flow becomes unstable. In contrast, the smallest positive eigenvalues cause an initial decay of disturbances, indicating that the flow is stable and physically meaningful. Moreover, the Σ_d is positive for upper branch solution; hence, it is stable and physically reliable, while the lower branch is unstable due to the negative eigenvalues.

Table 5: The smallest eigenvalues Σ_d at selected values of the unsteadiness parameter β_d

β_d	Upper Branch Solution	Lower Branch Solution
-1.18	2.7480	-1.4093
-1.10	2.6755	-1.4892
-1.00	2.5914	-1.5698
-0.90	2.5136	-1.6385
-0.80	2.4417	-1.6999

Tables 6 and 7 display the test of grid independence for the values of the dimensionless velocity and temperature profiles using the sundry choice of the step size h when $f_{wd} = 1.6$, $\beta_d = -2.0$, $\lambda_d = -2.5$,$\mathrm{Pr} = 6.2$, $R_{radd} = 2.0$, $Ec_d = 0.5$, $M_d = 0.1$, $\varphi_{np} = 0.03$, $K_d = 0.5$, and $Bi_d = 0.5$. The grid independence test is carried out for the upper and lower branch solutions. In addition, it is observed that the both branches outcomes are in good agreement.

Table 6: The grid independence test for the upper branch solution using a different values of step size h

Function	h	ξ					
		0.0	1.0	2.0	3.0	4.0	5.0
$G'(\xi)$	30.0	−2.5000	0.9270	0.9994	1.0000	1.0000	1.0000
	60.0	−2.5000	0.9299	0.9993	1.0000	1.0000	1.0000
	90.0	−2.5000	0.9355	0.9992	1.0000	1.0000	1.0000
$S(\xi)$	30.0	0.1788	0.0023	0.0000	0.0000	0.0000	0.0000
	60.0	0.1787	0.0022	0.0000	0.0000	0.0000	0.0000
	90.0	0.1786	0.0019	0.0000	0.0000	0.0000	0.0000

Table 7: The grid independence test for the lower branch solution using a different values of step size h

Function	h	ξ					
		0.0	1.0	2.0	3.0	4.0	5.0
$G'(\xi)$	30.0	−2.5000	−1.1718	0.5935	0.9644	0.9996	1.0000
	60.0	−2.5000	−1.3412	0.4905	0.9616	0.9994	1.0000
	90.0	−2.5000	−1.3576	0.5069	0.9594	0.9992	1.0000
$S(\xi)$	30.0	0.0031	−0.2227	−0.0314	−0.0006	0.0000	0.0000
	60.0	0.0031	−0.2314	−0.0437	−0.0007	0.0000	0.0000
	90.0	0.0031	−0.2321	−0.0416	−0.0008	0.0000	0.0000

6 Advanced Machine Learning Techniques for Surrogate Modeling

The bvp4c solver provides precise and reliable simulations for fluid dynamics, it is prohibitively expensive to use on a large scale and in situations where speed is of the essence. Data-driven surrogate modelling techniques are being studied to alleviate this concern. For instance, although ANNs traditionally apply the Levenberg-Marquardt Algorithm to train ANNs on Datasets used for fluid dynamic modelling, fewer studies have compared ANNs trained using Adam or GPR as modern alternatives. This paper compares multiple state-of-the-art surrogate modelling techniques. We compare the performance of various models, such as ANN with Adam optimizer or Levenberg-Marquardt and compare with Gaussian Process Regression in predicting the skin-friction coefficient and Nusselt number associated with the unsteady motion of second-grade nanofluids subjected to Joule Heating. The goal of this study is to find out which method offers better accuracy and reliability.

6.1 Artificial Neural Network (ANN) Modeling

Artificial neural networks (ANNs) use connected "neurons" to learn complex data patterns, especially when these patterns are hard to describe with equations. In this study, we modelled with a standard feedforward ANN (Fig. 12) and used a grid search to choose the best number of neurons in the hidden layer. We focused on training methods rather than network structure, testing two

optimization approaches: Levenberg–Marquardt, which speeds up training on small tasks, and Adam, which works better on larger datasets and models. We studied how each method impacts accuracy and performance on new data.

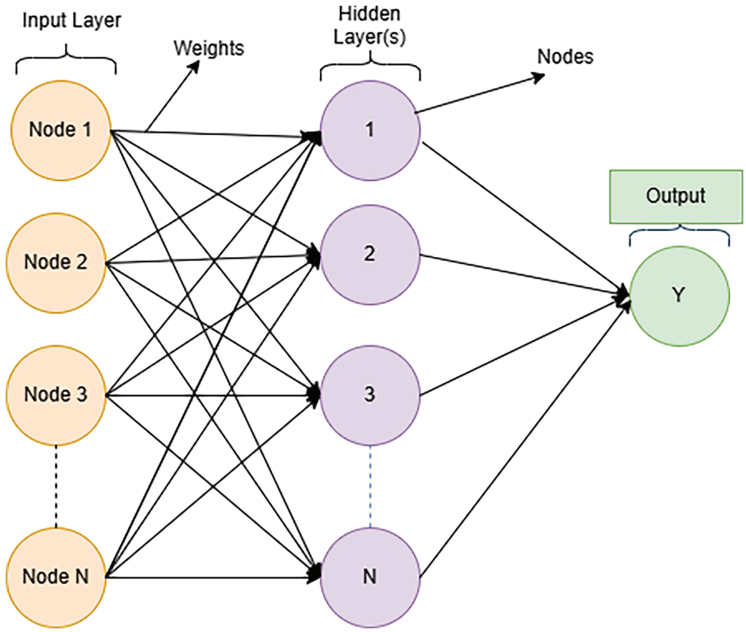

Figure 12: Architecture of the feedforward artificial neural network

ANN Algorithms

The Levenberg-Marquardt method is a powerful tool for solving problems like non-linear least squares (Levenberg [40], Marquardt [41]). It uses two methods at the same time: distant from the optimal answer, it behaves like slower, steady gradient descent; closer to the solution, it changes to the quicker Gauss-Newton approach, which employs more information to arrive at the conclusion immediately. This makes LM fast and reliable for training small to medium-sized networks for regression problems, However, it can cost too much to use with large datasets (Hagan and Menhaj [42]). Adam is a powerful and popular method for training deep learning models. Adam essentially enhances the behaviour of traditional stochastic gradient descent by: (i) incorporating the use of momentum to assist with accelerating convergence while at the same time escaping local minimum and cure issues with the optimization landscape; (ii) through updating each parameter's learning rate according to an exponentially weighted average over time of each parameter's past squared gradients (Kingma and Ba [43]). Therefore, Adam can apply a greater learning rate to parameters that experience small gradients and reduce the learning rate for those that experience larger or more erratic gradients, which contributes to the success of Adam in solving problems, particularly when applied to large datasets and complex models.

6.2 Gaussian Process Regression (GPR) Modeling

Gaussian Process Regression is a flexible Bayesian method that does not assume a fixed model shape, which provides a full distribution of functions that could best fit a given dataset instead of just one best fit function (Jagan et al. [44]). GPR assumes that the observed target variable can be modeled as if it was sampled from a Gaussian process; this is analogous to using a multivariate

normal distribution with an infinitely large number of observations. GPR provides both predictions and quantifies the uncertainty associated with these predictions. Therefore, because of this feature, GPR is well suited for use in reliability analysis and for design optimization (Le [45]). How well a GPR model works mostly depends on its kernel, which checks how similar the data points are (Zhang and Xu [46]). We tested four kernels to find which worked best for our problem, as shown in Fig. 13.

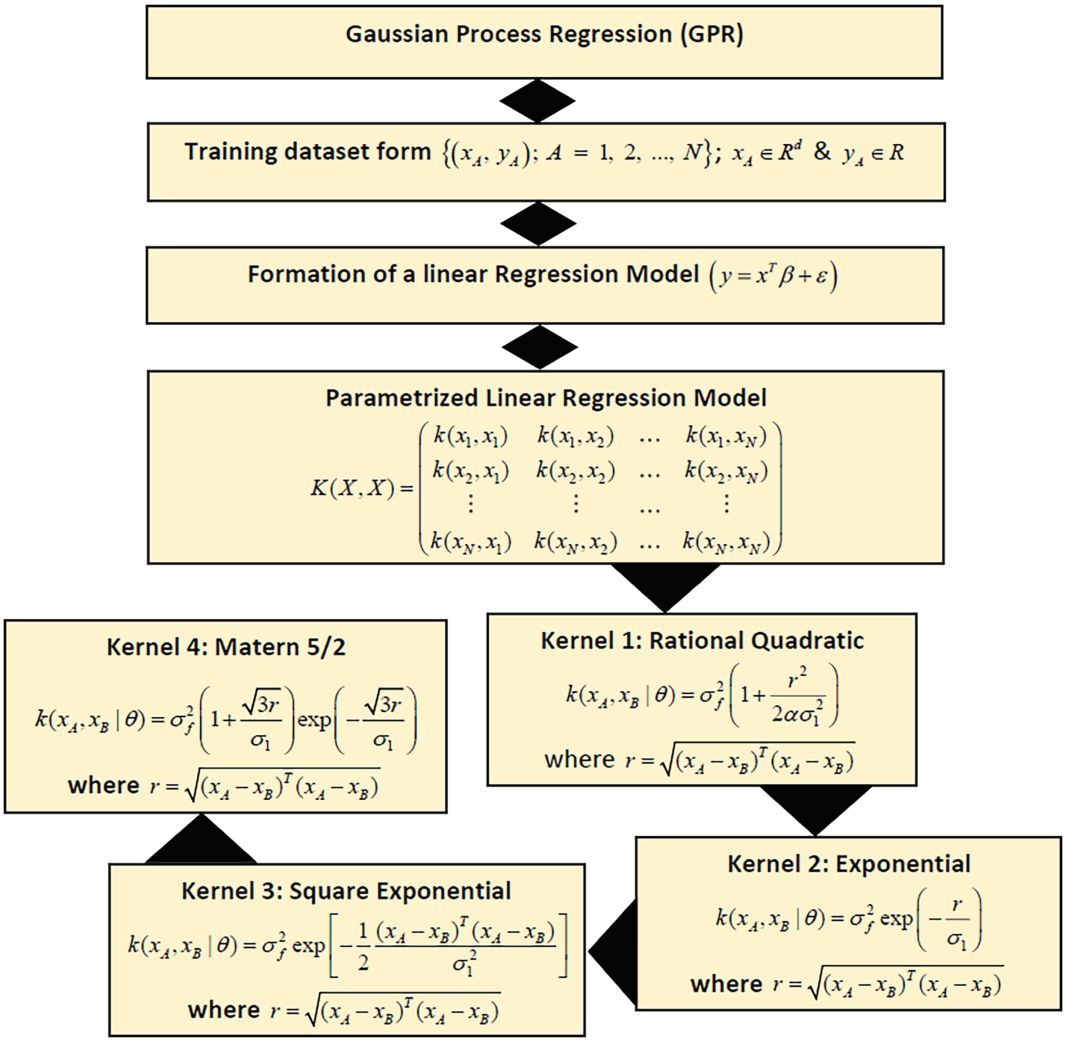

Figure 13: Illustration of gaussian process regression

GPR Kernels

A squared exponential is an extremely flexible function. The most important advantage of the squared exponential kernel is that it can perform kernel tricks which helps to avoid direct inner product calculations and large errors simultaneously, particularly with larger/complex/high-dimensional datasets. The squared exponential kernel is a very flexible radial basis function-like model. (Van Dao et al. [47]).

Computing costs and error rates will be lower when using these types of modelling methods, especially for large and complicated datasets (Zhang et al. [48]). The squared exponential and the

exponential kernels have similar properties; however, the metrics by which they measure distance are different. Squared distance is used for the squared exponential, whereas Euclidean distance is used for the exponential kernel (Zhang et al. [48]). Because of the use of the exponential kernel, users typically have more consistent results with fewer mistakes than if the squared exponential were used; however, there are some limitations to the ability to accurately detect sharp spikes or abrupt changes in the dataset. The Matérn 5/2 kernel is helpful because it lets us control how smooth the learned function is. It is linked to the RBF kernel and can be derived from it using Fourier transforms (Alghamdi et al. [49]), its extra parameter for tuning smoothness makes it especially helpful. If we expect a function to vary at several different rates, the rational quadratic kernel is a very good choice. It is like combining many smooth curve functions, each with its own rate of change. Together, they create a kernel that can adjust to many kinds of patterns.

6.3 Dataset Description, Preprocessing, and Reproducibility

The dataset used for surrogate modeling was generated by repeatedly solving the similarity system (8)–(9) subject to (10) using MATLAB bvp4c. Each run corresponds to one set of dimensionless physical inputs and produces target outputs for the posited skin friction coefficient and Nusselt number. Only converged numerical solutions were retained. In total, 1809 converged samples were collected for machine learning analysis. The dataset was randomly split using a fixed seed into 70% training, 15% validation, and 15% testing. Hyperparameters were tuned using the validation set only, and final performance was reported on the held-out test set. All experiments were performed in MATLAB.

6.3.1 Training and Model Performance Evaluation

A systematic, reproducible process for training and testing models was developed so that comparisons would be meaningful and fair for all of the models. A fixed seed for randomness was employed to ensure reproducibility of results. For this purpose, the 1809 unique samples were randomly split to three groups (70% for training, 15% for validation, and 15% for testing on unknown). Each model's settings were specifically tuned to maximize performance by reducing overfitting (i.e., when a model "learns" the training data rather than learning from it). For ANN model types, grid search was performed to identify the optimal number of hidden neurons (in the range of 16 to 200). For GPR model types, we evaluated multiple kernels and selected the version with the lowest RMSE out of the validation sample.

6.3.2 Models Evaluation Measures

We checked each model's performance with four common statistics that show how well they predict and works on new data. These measures are defined by the following formulas:

Coefficient of Determination (R^2): This tells us how well the input features can explain changes in the target variable. Numbers closer to 1 show that the model fits the data more closely. Thus,

$$R^2 = 1 - \frac{\sum_{j=1}^{n} \left(N_{numerical(j)} - N_{predicted(j)}\right)^2}{\sum_{j=1}^{n} \left(N_{numerical(j)} - \overline{N}_{numerical(j)}\right)^2}. \tag{28}$$

Mean Squared Error (MSE): It calculates the average of the squared differences between the predicted values and the actual values. This measure can easily be affected by large errors. So,

$$MSE = \frac{1}{n}\sum_{j=1}^{n}\left(N_{numerical(j)} - N_{predicted(j)}\right)^2. \tag{29}$$

Root Mean Squared Error (RMSE): RMSE is a way to measure prediction errors using the same units as the target value. It tells you, on average, how far the predictions are from the real values, and it is calculated as the square root of the MSE.

$$RMSE = \sqrt{\frac{1}{n}\sum_{j=1}^{n}\left(N_{numerical(j)} - N_{predicted(j)}\right)^2}. \tag{30}$$

Mean Absolute Error (MAE): It quantifies the magnitude of the error by computing the mean of the absolute differences between the predicted and actual values.

$$MAE = \frac{1}{n}\sum_{j=1}^{n}\left|N_{numerical(j)} - N_{predicted(j)}\right|. \tag{31}$$

In above Eqs. (28)–(31), $N_{numerical(j)}$ represents the values that were actually recorded (actual or observed) $N_{predicted(j)}$ is the predicted values, $\overline{N}_{numerical(j)}$ stands for the average of the measured values, while n indicates how many data points are included in the dataset.

7 Analysis of the Advanced Machine Learning Results

We carried out a comprehensive set of tests to create and validate models that predict the skin friction coefficient and Nusselt number. We employed three distinct machine learning techniques: a neural network using the Adam optimizer, a neural network trained with the Levenberg-Marquardt optimizer, and a Gaussian process regression model. We trained and evaluated all models on a dataset, then selected the one achieving the smallest validation RMSE. The results of these trained models are below.

7.1 Evaluating Prediction of Skin Friction Coefficient

We checked how well the machine learning models could predict the skin friction coefficient using 1809 data samples: 1266 for training, 272 for validation, and 271 for testing. The results, shown in Tables 8 and 9, indicate that all models were very close to the reference values, with R^2 values higher than 0.9999 for all datasets. This means the chosen input features provide enough information for accurate prediction of skin friction.

Table 8 shows that the ANN trained with the Levenberg–Marquardt (LM) algorithm reached almost perfect accuracy on all data groups, with very small errors (Test RMSE = 0.000179 and MAE = 0.000112). The training, validation, and test errors are all low and similar, meaning the model works well on new data. So, the ANN–LM model with 128 neurons is the best setup for predicting skin friction in this dataset. In addition, Table 8 shows that the ANN trained with Adam and adjusted using Bayesian optimization did not perform quite as well as the ANN trained with the LM algorithm. Although it still gave very accurate predictions (Test $R^2 = 0.999982$), its error values were clearly higher (Test RMSE = 0.047655, MAE = 0.031037). In addition, the validation RMSE (0.074727) exceeded the training RMSE (0.064083), suggesting that the model does not generalize as effectively and is

more sensitive to changes in its settings and optimization process. Overall, the Adam-based ANN is a workable option, but it is less effective than the LM-trained ANN for this particular problem.

Table 8: ANN model performance for the skin friction coefficient

Model	Algorithm	Dataset Type	Statistical Performance Measures			
			R^2	RMSE	MSE	MAE
ANN	**Adam** (Bayesian Optimization) with 2 layers (149–10), learning rate = 1.09×10^{-3}	Training	0.999977	0.064083	0.004107	0.038930
		Validation	0.999974	0.074727	0.005584	0.044656
		Testing	0.999982	0.047655	0.002271	0.031037
ANN	**LM** with 128 neurons	Training	1.000000	0.000193	0.000000	0.000113
		Validation	1.000000	0.000224	0.000000	0.000124
		Testing	1.000000	0.000179	0.000000	0.000112

Table 9: GPR model performance for the skin friction coefficient

Model	Kernel	Dataset Type	Statistical Performance Measures			
			R^2	RMSE	MSE	MAE
GPR	Rational quadratic	Training	0.999999	0.009416	0.000089	0.005150
		Validation	0.999999	0.010639	0.000113	0.005968
		Testing	1.000000	0.007299	0.000053	0.004386
	Matern 5/2	Training	0.999980	0.059295	0.003516	0.030781
		Validation	0.999980	0.066629	0.004439	0.034223
		Testing	0.999979	0.050859	0.002587	0.028876
	Squared exponential	Training	0.999988	0.046719	0.002183	0.026968
		Validation	0.999989	0.049982	0.002498	0.028926
		Testing	0.999989	0.037498	0.001406	0.022446
	Exponential	Training	1.000000	0.003035	0.000009	0.001161
		Validation	0.999998	0.018327	0.000336	0.004166
		Testing	0.999998	0.015591	0.000243	0.004785

Based on the results presented in Table 9, it is clear that the selection of an appropriate kernel will have a significant effect on the accuracy of predictions made with the selected kernel. The rational quadratic kernel was found to provide the highest overall performance compared to the other selection of kernels. The Validation RMSE for the rational quadratic kernel was 0.010639, while the RMSE for

the Test data set was 0.007299. The rational quadratic kernel also represents the best non-parametric choice among the four considered. The exponential kernel had a relatively low Validation RMSE of 0.018327, while both the squared exponential and Matern 5/2 kernels produced larger Validation RMSEs (0.049982 and 0.066629, respectively). The exponential kernel produced the lowest Training RMSE compared to all other kernels, but the Validation RMSEs of the exponential kernel were larger than the Validation RMSEs of the rational quadratic kernel, demonstrating that the rational quadratic kernel represents a better generalization when applied to previously unseen data.

Overall, the ANN-LM model had both the best overall prediction accuracy across the entire 1809 sample dataset and also showed the most stability. The GPR model that performed the best was using the rational quadratic kernel. While the ANN-Adam method had high R^2 values, it produced a greater number of predicted errors when compared to the ANN-LM and the best Gaussian process model kernel. Therefore, the ANN-Adam method is less accurate than either the ANN-LM or GPR methods when estimating skin friction coefficients.

7.2 GPR Graphs for the Skin Friction Coefficient

Several diagnostic plots are generated for the best GPR model (rational quadratic kernel) for skin friction prediction. As shown in Table 9, this kernel gave the highest accuracy, with R^2 of 0.999999 for training and validation and 1.000000 for testing, and very low errors (Validation RMSE = 0.010639; Test RMSE = 0.007299). The plots show well-tuned hyperparameters, close agreement between predictions and actual values, the error spread, and prediction confidence. They also show that this kernel outperforms the exponential, squared exponential, and Matern 5/2 kernels, which have higher validation and test errors.

Fig. 14 illustrates the hyperparameter optimization progress for the rational quadratic GPR kernel over 30 iterations, using a logarithmic scale for the cross-validated MSE. While some iterations have higher errors (showing active exploration), the optimizer quickly finds a low-error area (about 10^{-4}) and keeps returning to it. The concentration of later iterations close to the dashed minimum line indicates a strong convergence to a good hyperparameter setting.

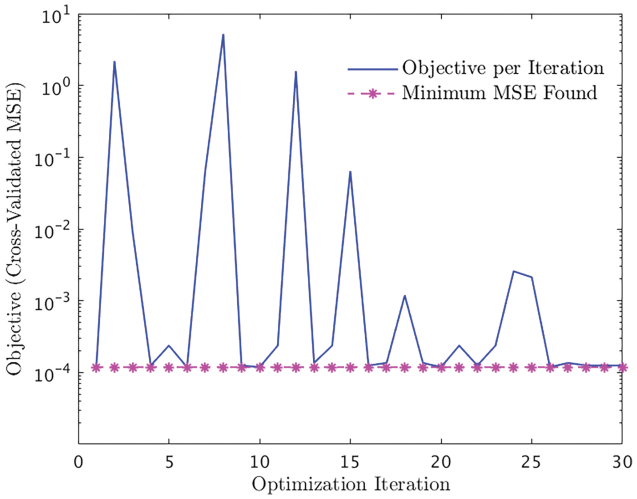

Figure 14: GPR Hyperparameter optimization progress

The accuracy of the final optimized GPR model is shown in the regression analysis plot in Fig. 15. This plot displays the predicted values compared to the actual values for the training, validation, and test sets. The points closely follow the 45-degree line, confirming the R^2 value of 1.0000. This shows a very strong fit and great ability to generalize from the training data to the test data.

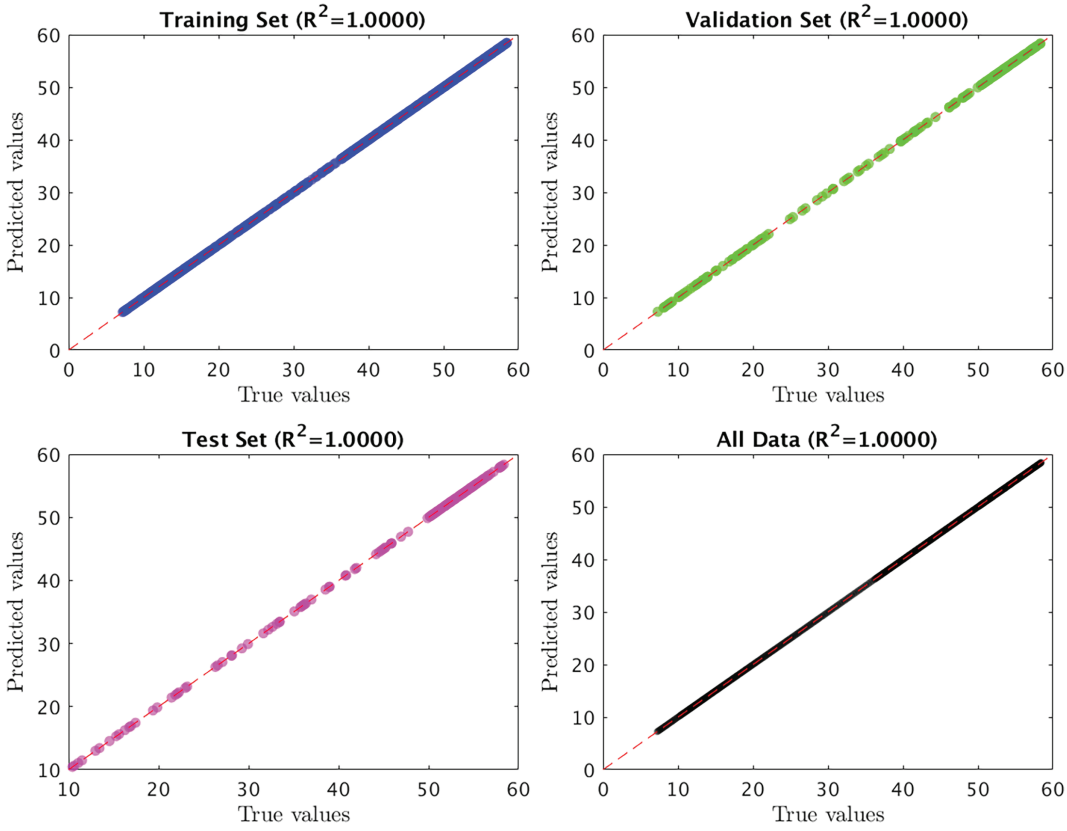

Figure 15: GPR regression analysis for training, validation, test, and all data sets

The error histogram in Fig. 16 shows how far the model's predictions are from the actual values in the test set. It has a tall, narrow peak at zero, meaning most errors are small and the model performs reasonably well. The sharp drop from zero shows that large errors are uncommon. The residual plot, which can be seen in Fig. 17, shows us how closely the model matches the values that it predicted. In general, the pattern of the errors appears to be random, meaning that the model has probably produced a good result, and also indicates that the variance in the errors (homoscedasticity) is a constant and does not change over time. At the highest end of our predicted value range (>45), there is an increase in the variability of the errors in an upward direction which indicates there may be a very slight tendency towards underpredicting but again we still have very small error numbers. One of the strengths of GPR is the ability to quantify the uncertainty of our predictions, as shown in Fig. 18. In this plot, we show the actual test values sorted to provide a clearer view, the GPR predicted values shown next to the actuals and the 95% confidence intervals for each GPR prediction. The confidence band is extremely tight around all the predicted values and is almost coincident with the actual value line for all points in the data set. This indicates the model has high certainty in its predictions, making it a reliable tool for engineering use.

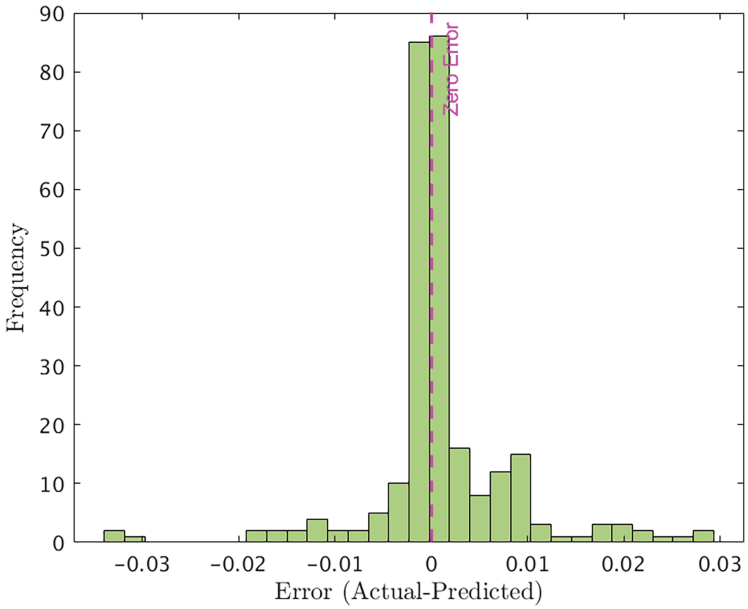

Figure 16: Error histogram for the GPR model on the test set for the skin friction coefficient prediction

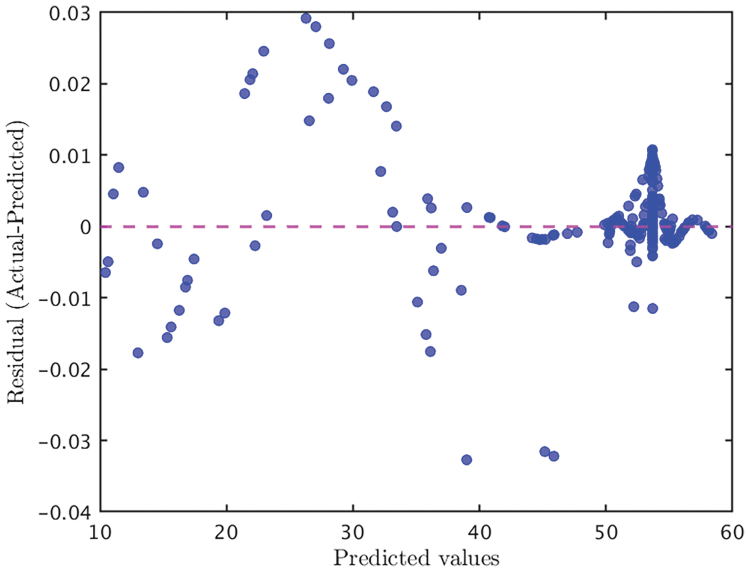

Figure 17: Residuals vs. predicted values for the GPR model on the test set for the skin friction coefficient prediction

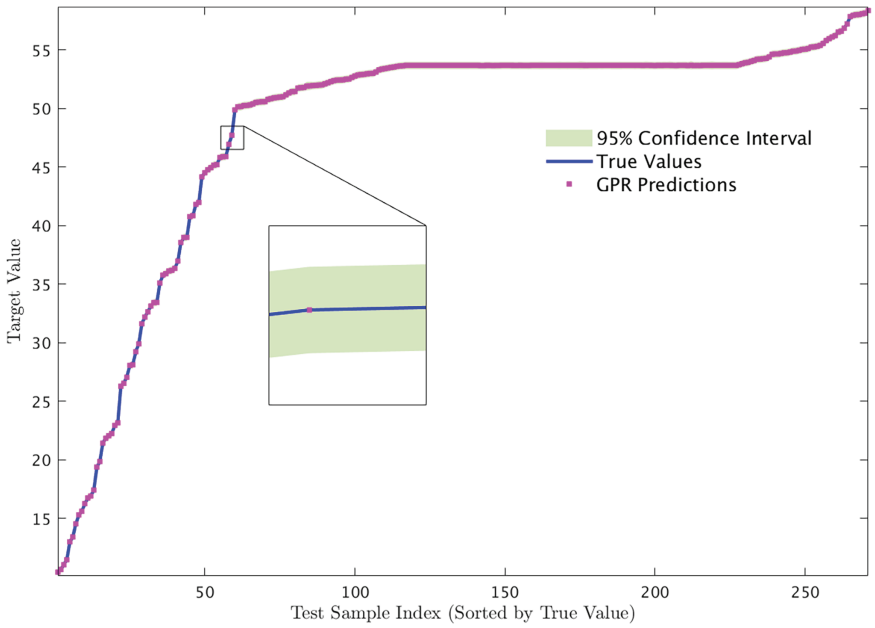

Figure 18: Sorted predictions vs. true values of the skin friction coefficient with 95% confidence intervals for the GPR model

7.3 Evaluating the Prediction of Nusselt Number Coefficient

A parallel evaluation was carried out to test how well the developed machine learning models predicted the Nusselt number (Nu), and the results are shown in Tables 10 and 11. All models performed very well, with R^2 values of 0.9999 or higher for most training, validation, and testing sets, showing that they accurately captured the Nu relationship from the selected inputs. As shown in Table 10, the ANN model using the Levenberg–Marquardt (LM) algorithm with 96 neurons gave the best results, with nearly perfect performance in all sets, a very low test RMSE of 3.0×10^{-5}, and little error variation, indicating strong reliability and generalization. The Adam-based ANN, tuned with Bayesian search, showed larger prediction errors despite a strong fit (test $R^2 = 0.999924$) and a test RMSE of 6.046×10^{-3}, making it less accurate than the LM-trained model. The GPR results in Table 11 show that the choice of kernel greatly affects model performance: the Matern 5/2 kernel provided the best overall results with a low test RMSE of 4.70×10^{-4}. The rational quadratic and squared exponential kernels followed closely, while the exponential kernel had the smallest training error but the highest test error (RMSE $= 1.062 \times 10^{-3}$), showing weaker generalization. Overall, these results indicate that the ANN–LM is the most accurate method for predicting the Nusselt number in this dataset, while GPR with the Matern 5/2 kernel is the best non-parametric alternative.

Table 10: ANN model performance for the Nusselt number

Model	Algorithm	Dataset Type	Statistical Performance Measures			
			R^2	RMSE	MSE	MAE
ANN	Adam (Bayesian Opt.) best params: 1 layer (200), learning rate = 2.81×10^{-3}	Training	0.999938	0.005145	0.000026	0.003531
		Validation	0.999929	0.005509	0.000030	0.003720
		Testing	0.999924	0.006046	0.000037	0.004005
ANN	LM with 96 neurons	Training	1.000000	0.000028	0.000000	0.000024
		Validation	1.000000	0.000028	0.000000	0.000024
		Testing	1.000000	0.000030	0.000000	0.000026

Table 11: GPR model performance for the Nusselt number

Model	Kernel	Dataset Type	Statistical Performance Measures			
			R^2	RMSE	MSE	MAE
GPR	Rational quadratic	Training	0.999999	0.000601	0.000000	0.000298
		Validation	0.999999	0.000629	0.000000	0.000320
		Testing	0.999999	0.000678	0.000000	0.000334
	Matern 5/2	Training	1.000000	0.000431	0.000000	0.000168
		Validation	1.000000	0.000438	0.000000	0.000183
		Testing	1.000000	0.000470	0.000000	0.000189
	Squared exponential	Training	0.999999	0.000675	0.000000	0.000343
		Validation	0.999999	0.000707	0.000001	0.000365
		Testing	0.999999	0.000761	0.000001	0.000383
	Exponential	Training	1.000000	0.000164	0.000000	0.000038
		Validation	1.000000	0.000265	0.000000	0.000098
		Testing	0.999998	0.001062	0.000001	0.000192

7.4 GPR Graphs for the Nusselt Number

A parallel diagnostic analysis was conducted on the best GPR model with a Matern 5/2 kernel for predicting the Nusselt number, as shown in Figs. 19–23. Fig. 19 displays the hyperparameter optimization trace for the Nusselt number model. Similar to the skin friction model, the optimization successfully explored and quickly found a spot with very low cross-validated MSE. The repeated identification of this high-performance area over 30 iterations shows that the final hyperparameter choice is reliable.

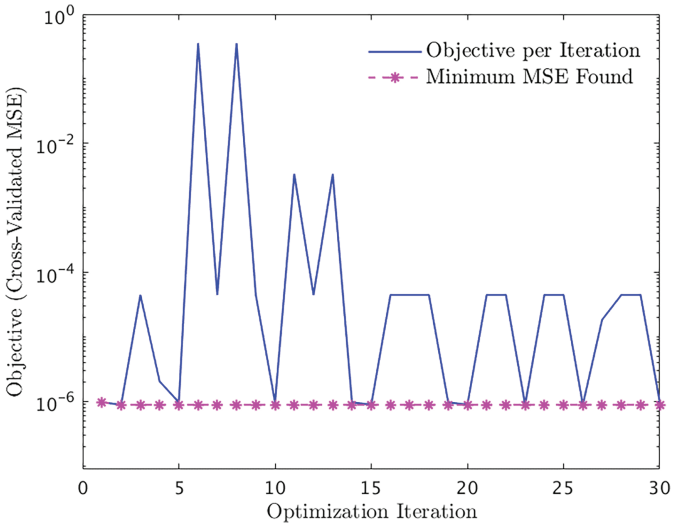

Figure 19: GPR Hyperparameter optimization progress for Nusselt number prediction

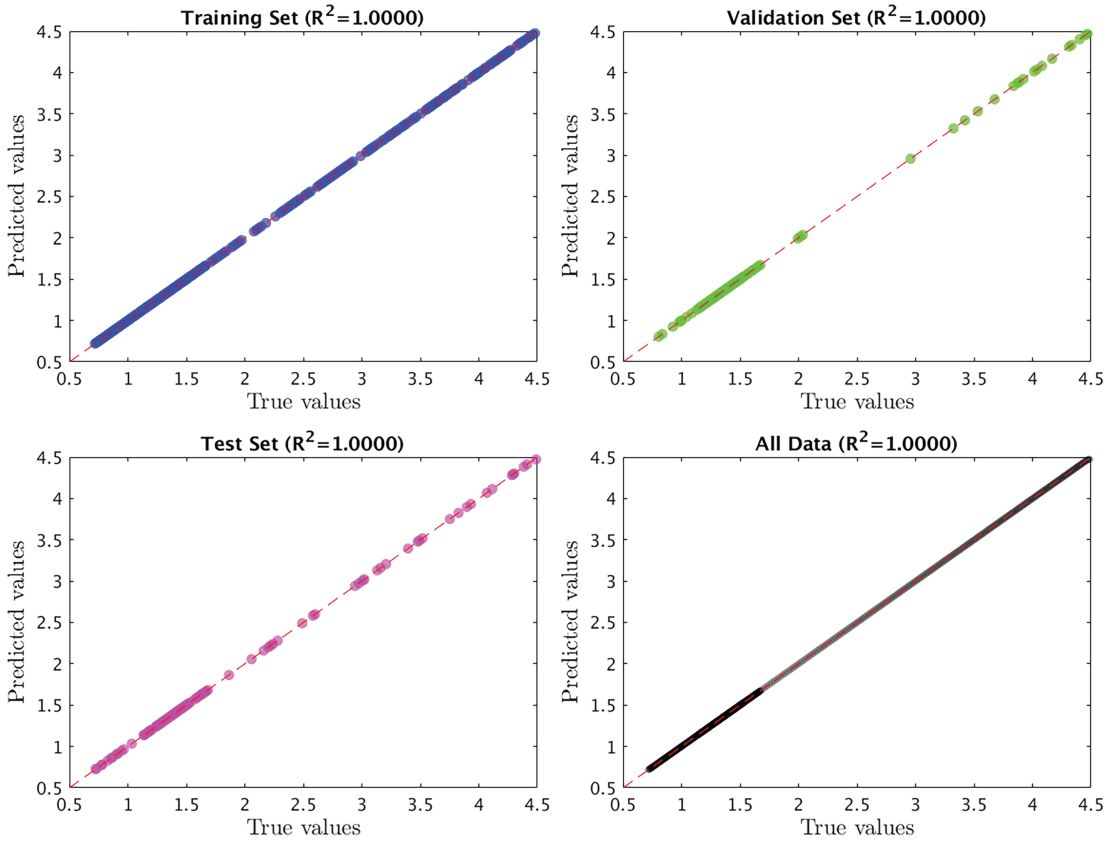

Figure 20: GPR Regression analysis for training, validation, and test sets for Nusselt number prediction

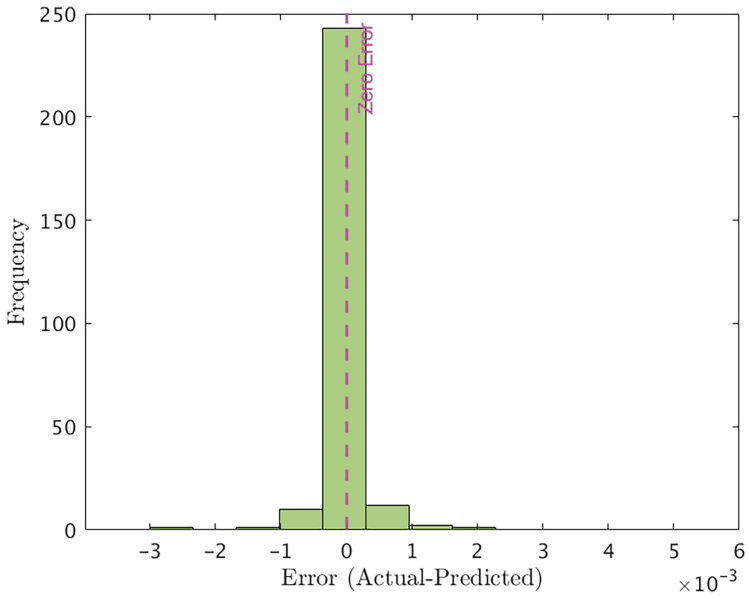

Figure 21: Error histogram for the GPR model on the test set for Nusselt number prediction

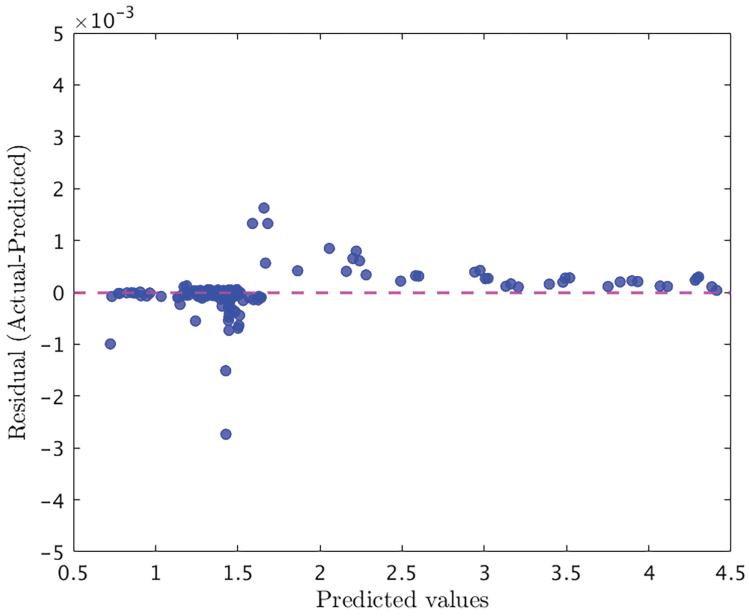

Figure 22: Residuals vs. predicted values for the GPR model on the test set for the Nusselt number prediction

As seen in Fig. 20, the GPR model has been optimally fitted based on a regression with an exact R^2 score of 1.0000 across all data groups, indicating that the predicted results track tightly along the 45° diagonal line, highlighting the precision of this model. Essentially, these results demonstrate the ability of the GPR model to accurately depict the relationship between the variables in the data sample and successfully predict new observations based on this relationship.

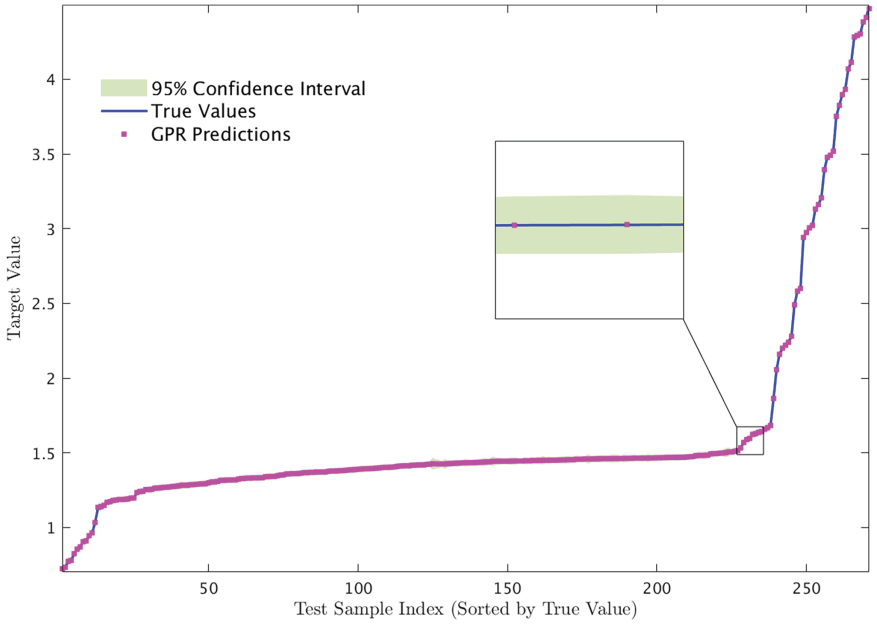

Figure 23: Sorted predictions vs. true values of the Nusselt number with 95% confidence intervals for the GPR model

Fig. 21 illustrates the frequency of errors related to testing and training occurred at very small values, as indicated by a spike in bar length on the histogram at zero, which produces a normal distribution. Because of this clear spike, there is no bias in the Nusselt number predictions. The residuals plot in Fig. 22 for the model shows a low level of correlation between error and predicted temperature values, it appears to be random in nature and does not reflect a specific pattern, which supports the stability and consistency of the prediction of the model across all values of Nusselt number. The GPR model's prediction confidence is shown in Fig. 23. The graph displays the true values from the test set, the GPR's predicted points, and the 95% confidence interval for each prediction. Like the skin friction model, the confidence band is very narrow and closely surrounds the true value line. This shows that the model is highly reliable for making predictions in thermal analysis.

7.5 On the Near-Perfect R^2 Values

A parallel evaluation was conducted to test how well the developed because the targets (Cf, Nu) are generated from a deterministic numerical solver for a fixed physics-based model, the input-output mapping can be highly smooth and low-noise within the sampled parameter ranges; therefore, very high R^2 values can occur even for genuinely generalizing models. Nevertheless, R^2 may also indicate leakage or overfitting if preprocessing uses information from validation/test data. To mitigate this risk, we (i) applied feature scaling using training statistics only, (ii) performed hyperparameter selection on the validation set only, and (iii) evaluated all reported metrics on a held-out test set not used in model fitting or tuning. Residual and error-distribution diagnostics (see Figs. 17 and 22) further indicate small, approximately unbiased errors across the test set. Future work will additionally report k-fold cross-validation and/or external validation under expanded parameter ranges to further stress-test generalization.

8 Final Remarks

The aim of the research is to scrutinize the time-dependent flow of a special kind of second-grade liquid through $CoFe_2O_4$ nanoparticles induced by a movable sheet. Also, the impact of Joule heating, the magnetic effect, and convective boundary conditions is provoked. Significant physical factors are employed to demonstrate the dual solutions, including the velocity, temperature, the skin friction, and the Nusselt number. In addition, this research also addressed important questions regarding machine learning in engineering fields. Whilst the excellent accuracy of ANN trained with the Levenberg-Marquardt algorithm is well documented, no earlier research has thoroughly quantified how this model such as the GPR and their intrinsic benefit of uncertainty assessment executes vs. this greater accuracy standard. This study was planned to measure that relationship. The following summarizes the important findings from our comparative and machine learning analysis:

- Dual solutions exist owing to unsteady parameters and moving parameters.
- The SF enhances the UB outcome and reduces the LB outcome; however, the heat transport noticeably augments both results.
- The separation of the boundary layer decelerates because of increasing values of the mass suction, magnetic, and second-grade factors.
- The impact of Eckert's number shows the increasing function of the temperature.
- The width of the thermal and momentum boundary layers dramatically changed due to the viscosity factor.
- The magnetic factor enhances the velocity distribution noticeably for the LB outcome and weakens for the UB outcome.
- This research discloses that the GPR is a commanding replacement for ANN, generating the LNN calculations with errors similar to the benchmark of ANN-LM and an R^2 of 1.000.
- The results make GPR a valuable tool for reliability analysis, risk measurement, and engineering design when calculation assurance is important because it enumerates improbability with no loss in precision.
- GPR and ANN-LM perform better than the ANN-Adam model, even though it is accurate. This shows that the main strength of ANN-Adam is its ability to handle larger datasets than those used.

Limitation

The present problem has the following limitation in the mechanism of the fluid flow, which has been outlined as:

- The present research includes the time-dependent flow towards a stagnation point.
- The Joule heating effect has been investigated.
- The flow is incompressible.
- The non-Newtonian modified second-grade fluid is considered.
- The irregular free stream velocity and convective boundary condition dependent on time have been invoked.

Acknowledgement: The authors received specific funding from Al-Balqa Applied University, Jordan.

Funding Statement: The authors received specific funding for this work from Al-Balqa Applied University, Jordan.

Author Contributions: Suad Alrebdi, Umair Khan: Conceptualization, methodology, software, formal analysis, validation; writing—original draft, data curation and visualization. Aurang Zaib: Conceptualization, writing–original draft, writing–review & editing, supervision and resources. Rania Saadeh: Validation, investigation, writing–review & editing, formal analysis, project administration and funding acquisition. All authors reviewed and approved the final version of the manuscript.

Availability of Data and Materials: The datasets used and/or analyzed during the current study are available from the corresponding author upon reasonable request.

Ethics Approval: Not applicable.

Conflicts of Interest: The authors declare no conflicts of interest.

Nomenclature

A_s, A_t	Rivlin-Ericksen tensors
B_0	Constant magnetic effect
Bi_d	Biot number
C_f	Skin friction
c_p	Specific heat (J K^{-1} kg^{-1})
Ec_d	Eckert number
f_{wd}	Mass velocity transpiration (m/s)
h_f	Heat transfer coefficient
h_f^*	Uniform heat transfer
$\mathbf{I}_s$	Identity tensor
l_d	Characteristic length
M_d	Magnetic parameter
Nu_{x_d}	Nusselt number
p_s	Pressure
Pr	Prandtl number
q_{rad}	Radiative heat flux (W/m^2)
Re_{x_d}	Local Reynolds number
R_{radd}	Radiation parameter
T_d	Temperature (1/K)
T_{wdf}	Variable temperature (1/K)
T_r	Reference temperature
T_∞	Free-stream constant temperature
$u_{wd}\,(x_d, t_d)$	Wall velocity (m/s)
$u_{ed}\,(x_d, t_d)$	Free stream velocity (m/s)
$v_{wd}\,(t_d)$	Mass flux velocity (m/s)
x_d, y_d	Cartesian coordinates (m)

Greek Letters

β_d	Unsteadiness factor
τ_{sd}	New dimensionless time
μ	Fluid dynamic viscosity
λ_d	Moving parameter
ρ	Density (kg/m^3)
k	Thermal conductivity (W/m K)
σ	Electrical conductivity (S/m)
γ_c,γ_d	Normal stresses moduli
γ_e	Unsteadiness with dimension (time)$^{-1}$
φ_{np}	Solid nanoparticles volume fraction
ψ	Stream function
ξ	Pseudo-similarity constraint

Superscripts

f	Convectional fluid
np	Nanoparticles
nf	Nanofluid

Abbreviations

GPR	Gaussian Process Regression
$CoFe_2O_4$	Magnetized cobalt ferrite
H_2O	Water
SG	Second grade
LNN	Local Nusselt number
SF	Skin friction

References

1. Rivlin R, Ericksen J. Stress-deformation relations for isotropic materials. Indiana Univ Math J. 1955;4(2):323–425. doi:10.1512/iumj.1955.4.54011.
2. Vajravelu K, Roper T. Flow and heat transfer in a second grade fluid over a stretching sheet. Int J Non Linear Mech. 1999;34(6):1031–6. doi:10.1016/S0020-7462(98)00073-0.
3. Vajravelu K, Rollins D. Hydromagnetic flow of a second grade fluid over a stretching sheet. Appl Math Comput. 2004;148(3):783–91. doi:10.1016/S0096-3003(02)00942-6.
4. Labropulu F, Li D. Stagnation-point flow of a second-grade fluid with slip. Int J Non Linear Mech. 2008;43(9):941–7. doi:10.1016/j.ijnonlinmec.2008.07.004.
5. Khan M, Rahman MU. Flow and heat transfer to modified second grade fluid over a non-linear stretching sheet. AIP Adv. 2015;5(8):087157. doi:10.1063/1.4929480.
6. Ramzan M, Bilal M, Farooq U, Chung JD. Mixed convective radiative flow of second grade nanofluid with convective boundary conditions: an optimal solution. Results Phys. 2016;6(1):796–804. doi:10.1016/j.rinp.2016.10.011.
7. Labropulu F, Li D. Unsteady stagnation-point flow of a second-grade fluid. J Fluid Flow Heat Mass Transf. 2016;3(1):17–24. doi:10.11159/jffhmt.2016.003.

8. Saif RS, Hayat T, Ellahi R, Muhammad T, Alsaedi A. Stagnation-point flow of second grade nanofluid towards a nonlinear stretching surface with variable thickness. Results Phys. 2017;7:2821–30. doi:10.1016/j.rinp.2017.07.062.
9. Awan AU, Abid S, Ullah N, Nadeem S. Magnetohydrodynamic oblique stagnation point flow of second grade fluid over an oscillatory stretching surface. Results Phys. 2020;18(7):103233. doi:10.1016/j.rinp.2020.103233.
10. Salahuddin T, Haider A, Alghamdi M. Unsteady squeezing second order of nanofluid flow through an infinite channel. Int J Numer Meth Heat Fluid Flow. 2021;31(11):3261–78. doi:10.1108/hff-03-2019-0197.
11. Khashi'ie NS, Waini I, Zokri SM, Kasim ARM, Arifin NM, Pop I. Stagnation point flow of a second-grade hybrid nanofluid induced by a Riga plate. Int J Numer Meth Heat Fluid Flow. 2022;32(7):2221–39. doi:10.1108/hff-08-2021-0534.
12. Hosseinzadeh K, Mardani MR, Paikar M, Hasibi A, Tavangar T, Nimafar M, et al. Investigation of second grade viscoelastic non-Newtonian nanofluid flow on the curve stretching surface in presence of MHD. Results Eng. 2023;17(4):100838. doi:10.1016/j.rineng.2022.100838.
13. Choi SUS, Eastman JA. Enhancing thermal conductivity of fluids with nanoparticles, developments and applications of Nan-Newtonian flows. In: Proceedings of the 1995 ASME International Mechanical Engineering Congress and Exposition; 1995 Nov 12–17; San Francisco, CA, USA. p. 99–105.
14. Mahdy A. Unsteady mixed convection boundary layer flow and heat transfer of nanofluids due to stretching sheet. Nucl Eng Des. 2012;249:248–55. doi:10.1016/j.nucengdes.2012.03.025.
15. Sheikholeslami M, Hayat T, Alsaedi A. MHD free convection of Al_2O_3-water nanofluid considering thermal radiation: a numerical study. Int J Heat Mass Transf. 2016;96(2):513–24. doi:10.1016/j.ijheatmasstransfer.2016.01.059.
16. Soid SK, Ishak A, Pop I. Boundary layer flow past a continuously moving thin needle in a nanofluid. Appl Therm Eng. 2017;114:58–64. doi:10.1016/j.applthermaleng.2016.11.165.
17. Kamal F, Zaimi K, Ishak A, Pop I. Stability analysis of MHD stagnation-point flow towards a permeable stretching/shrinking sheet in a nanofluid with chemical reactions effect. Sains Malays. 2019;48(1):243–50. doi:10.17576/jsm-2019-4801-28.
18. Al-Kouz W, Medebber MA, Elkotb MA, Abderrahmane A, Aimad K, Al-Farhany K, et al. Galerkin finite element analysis of Darcy-Brinkman–Forchheimer natural convective flow in conical annular enclosure with discrete heat sources. Energy Rep. 2021;7(4):6172–81. doi:10.1016/j.egyr.2021.09.071.
19. Khan U, Zaib A, Ishak A, Waini I, Sherif EM, Pop I. Analysis of jet wall flow and heat transfer conveying ZnO-SAE50 nano lubricants saturated in darcy-brinkman porous medium. Mathematics. 2022;10(17):3201. doi:10.3390/math10173201.
20. Khan U, Zaib A, Bashatah JA. ANN-based Levenberg-Marquardt backpropagation for optimizing melting heat transfer in non-Newtonian hybrid nanofluids. Multidisc Model Mater Struct. 2026;4(3):1–27. doi:10.1108/MMMS-08-2025-0319.
21. Yu Y, Khan U, Zaib A, Ishak A, Waini I, Raizah Z, et al. Exploration of 3D stagnation-point flow induced by nanofluid through a horizontal plane surface saturated in a porous medium with generalized slip effects. Ain Shams Eng J. 2023;14(2):101873. doi:10.1016/j.asej.2022.101873.
22. Elattar S, Khan U, Zaib A, Ishak A, Alwadai N, Albalawi H. Irreversible mechanism and thermal cross-radiative flow in nanofluids driven along a stretching/shrinking sheet with the existence of possible turning/critical points. Front Mater. 2024;11:1391066. doi:10.3389/fmats.2024.1391066.
23. Dawod AA, Khan U, Saadeh R, Zaib A, Ishak A, Waqas M, et al. Impact of gyrotactic microorganisms on 3D unsteady stagnation-point nanofluid flow across a plane horizontal surface with zero mass flux conditions. Alex Eng J. 2025;122(5):98–108. doi:10.1016/j.aej.2025.03.017.
24. Makinde OD, Aziz A. Boundary layer flow of a nanofluid past a stretching sheet with a convective boundary condition. Int J Therm Sci. 2011;50(7):1326–32. doi:10.1016/j.ijthermalsci.2011.02.019.

25. Alsaedi A, Awais M, Hayat T. Effects of heat generation/absorption on stagnation point flow of nanofluid over a surface with convective boundary conditions. Commun Nonlinear Sci Numer Simul. 2012;17(11):4210–23. doi:10.1016/j.cnsns.2012.03.008.
26. Ibrahim W. The effect of induced magnetic field and convective boundary condition on MHD stagnation point flow and heat transfer of upper-convected Maxwell fluid in the presence of nanoparticle past a stretching sheet. Propuls Power Res. 2016;5(2):164–75. doi:10.1016/j.jppr.2016.05.003.
27. Rasool G, Zhang T. Characteristics of chemical reaction and convective boundary conditions in Powell-Eyring nanofluid flow along a radiative Riga plate. Heliyon. 2019;5(4):e01479. doi:10.1016/j.heliyon.2019.e01479.
28. Baitharu AP, Sahoo S, Dash GC. Convective boundary layer flow and heat transfer of polar fluid in vertical concentric annuli with thermal slip. Int J Ambient Energy. 2022;43(1):4569–77. doi:10.1080/01430750.2021.1914162.
29. Rashad AM, Nafe MA, Eisa DA. Heat variation on MHD Williamson hybrid nanofluid flow with convective boundary condition and Ohmic heating in a porous material. Sci Rep. 2023;13(1):6071. doi:10.1038/s41598-023-33043-z.
30. Ahmed MF, Zaib A, Ali F, Khan U, Zafar SS. Thermal radiation of Walter-B magneto bioconvection nanofluid due to the stretching surface under convective condition and heat source/sink:a semi-analytical technique for the stagnation point. J Radiat Res Appl Sci. 2025;18(1):101291. doi:10.1016/j.jrras.2025.101291.
31. Mahabaleshwar US, Maranna T, Sofos F. Analytical investigation of an incompressible viscous laminar Casson fluid flow past a stretching/shrinking sheet. Sci Rep. 2022;12(1):18404. doi:10.1038/s41598-022-23295-6.
32. Goud Bejawada S, Dharmendar Reddy Y, Jamshed W, Nisar KS, Alharbi AN, Chouikh R. Radiation effect on MHD Casson fluid flow over an inclined non-linear surface with chemical reaction in a Forchheimer porous medium. Alex Eng J. 2022;61(10):8207–20. doi:10.1016/j.aej.2022.01.043.
33. Swain S, Sarkar GM, Sahoo B. Dual solutions and linear temporal stability analysis of mixed convection flow of non-Newtonian special third grade fluid with thermal radiation. Int J Therm Sci. 2023;189(2):108262. doi:10.1016/j.ijthermalsci.2023.108262.
34. Swain S, Sarkar GM, Sahoo B. Stability analysis of MHD stagnation point flow of Casson fluid past a shrinking sheet in porous medium considering heat sink or source, thermal radiation and suction effects. J Comput Sci. 2024;75(4):102207. doi:10.1016/j.jocs.2023.102207.
35. Adilakshmi V, Ramana Reddy GV, Kumar T, Mubaraki AM, Sambas A, Sulaiman IM. Radiation and diffusion effects on MHD Sisko fluid flow over a nonlinearly stretchable porous sheet. J Radiat Res Appl Sci. 2025;18(2):101541. doi:10.1016/j.jrras.2025.101541.
36. Fosdick RL, Rajagopal KR. Anomalous features in the model of “second order fluids”. Arch Ration Mech Anal. 1979;70(2):145–52. doi:10.1007/BF00250351.
37. Roy NC, Pop I. Flow and heat transfer of a second-grade hybrid nanofluid over a permeable stretching/shrinking sheet. Eur Phys J Plus. 2020;135(9):768. doi:10.1140/epjp/s13360-020-00788-9.
38. Harris SD, Ingham DB, Pop I. Mixed convection boundary-layer flow near the stagnation point on a vertical surface in a porous medium: brinkman model with slip. Transp Porous Medium. 2009;77(2):267–85. doi:10.1007/s11242-008-9309-6.
39. Bhattacharyya K. Dual solutions in boundary layer stagnation-point flow and mass transfer with chemical reaction past a stretching/shrinking sheet. Int Commun Heat Mass Transf. 2011;38(7):917–22. doi:10.1016/j.icheatmasstransfer.2011.04.020.
40. Levenberg K. A method for the solution of certain non-linear problems in least squares. Q Appl Math. 1944;2(2):164–8. doi:10.1090/qam/10666.
41. Marquardt DW. An algorithm for least-squares estimation of nonlinear parameters. J Soc Ind Appl Math. 1963;11(2):431–441. doi:10.1137/0111030.

42. Hagan MT, Menhaj MB. Training feedforward networks with the Marquardt algorithm. IEEE Trans Neural Netw. 1994;5(6):989–93. doi:10.1109/72.329697.
43. Kingma DP, Ba J. Adam: a method for stochastic optimization. arXiv:1412.6980. 2014.
44. Jagan J, Samui P, Kim D. Reliability analysis of simply supported beam using GRNN, ELM and GPR. Struct Eng Mech. 2019;71(6):739–49. doi:10.4018/978-1-4666-9619-8.ch030.
45. Le TT. Practical machine learning-based prediction model for axial capacity of square CFST columns. Mech Adv Mater Struct. 2022;29(12):1782–97. doi:10.1080/15376494.2020.1839608.
46. Zhang Y, Xu X. Relative cooling power modeling of lanthanum manganites using Gaussian process regression. RSC Adv. 2020;10(35):20646–53. doi:10.1039/d0ra03031g.
47. Van Dao D, Adeli H, Ly HB, Le LM, Le VM, Le TT, et al. A sensitivity and robustness analysis of GPR and ANN for high-performance concrete compressive strength prediction using a Monte Carlo simulation. Sustainability. 2020;12(3):830. doi:10.3390/su12030830.
48. Zhang N, Xiong J, Zhong J, Leatham K. Gaussian process regression method for classification for high-dimensional data with limited samples. In: Proceedings of the 2018 Eighth International Conference on Information Science and Technology (ICIST); 2018 Jun 30–Jul 6; Cordoba, Spain. p. 358–63. doi:10.1109/ICIST.2018.8426077.
49. Alghamdi AS, Polat K, Alghoson A, Alshdadi AA, Abd El-Latif AA. Gaussian process regression (GPR) based non-invasive continuous blood pressure prediction method from cuff oscillometric signals. Appl Acoust. 2020;164(11):107256. doi:10.1016/j.apacoust.2020.107256.